The Astrophysical Journal, 817:85 (25pp), 2016 February 1 doi:10.3847/0004-637X/817/2/85

THE DETECTION AND STATISTICS OF GIANT ARCS BEHIND CLASH CLUSTERS

Bingxiao Xu[1], Marc Postman[2], Massimo Meneghetti[3], Stella Seitz[4], Adi Zitrin[5,11], Julian Merten[6], Dani Maoz[7], Brenda Frye[8], Keiichi Umetsu[9], Wei Zheng[1], Larry Bradley[2], Jesus Vega[10], and Anton Koekemoer[3]
[1] Department of Physics and Astronomy, The Johns Hopkins University, 3400 North Charles Street, Baltimore, MD 21218, USA; bxu6@jhu.edu
[2] Space Telescope Science Institute, 3700 San Martin Drive, Baltimore, MD 21208, USA
[3] INAF, Osservatorio Astronomico di Bologna, & INFN, Sezione di Bologna; Via Ranzani 1, I-40127 Bologna, Italy
[4] Universitaets-Sternwarte, Fakultaet fuer Physik, Ludwig-Maximilians Universitaet Muenchen, Scheinerstr. 1, D-81679 Muenchen, Germany
[5] California Institute of Technology, MC 249-17, Pasadena, CA 91125, USA
[6] University of Oxford, Department of Physics, Denys Wilkinson Building, Keble Road, Oxford, OX1 3RH, UK
[7] School of Physics and Astronomy, Tel Aviv University, Tel-Aviv 69978, Israel
[8] Steward Observatory/Department of Astronomy, University of Arizona, 933 N. Cherry Ave., Tucson, AZ 85721, USA
[9] Institute of Astronomy and Astrophysics, Academia Sinica, P.O. Box 23-141, Taipei 10617, Taiwan
[10] Universidad Autonoma de Madrid, Ciudad Universitaria de Cantoblanco, E-28049 Madrid, Spain
Received 2015 June 26; accepted 2015 November 7; published 2016 January 22

ABSTRACT

We developed an algorithm to find and characterize gravitationally lensed galaxies (arcs) to perform a comparison of the observed and simulated arc abundance. Observations are from the Cluster Lensing And Supernova survey with Hubble (CLASH). Simulated CLASH images are created using the MOKA package and also clusters selected from the high-resolution, hydrodynamical simulations, MUSIC, over the same mass and redshift range as the CLASH sample. The algorithm's arc elongation accuracy, completeness, and false positive rate are determined and used to compute an estimate of the true arc abundance. We derive a lensing efficiency of 4 ± 1 arcs (with length $\geqslant 6''$ and length-to-width ratio $\geqslant 7$) per cluster for the X-ray-selected CLASH sample, 4 ± 1 arcs per cluster for the MOKA-simulated sample, and 3 ± 1 arcs per cluster for the MUSIC-simulated sample. The observed and simulated arc statistics are in full agreement. We measure the photometric redshifts of all detected arcs and find a median redshift $z_s = 1.9$ with 33% of the detected arcs having $z_s > 3$. We find that the arc abundance does not depend strongly on the source redshift distribution but is sensitive to the mass distribution of the dark matter halos (e.g., the c–M relation). Our results show that consistency between the observed and simulated distributions of lensed arc sizes and axial ratios can be achieved by using cluster-lensing simulations that are carefully matched to the selection criteria used in the observations.

Key words: galaxies: clusters: general – gravitational lensing: strong – methods: numerical – methods: observational – methods: statistical

1. INTRODUCTION

The occurrence frequency of giant gravitationally lensed arcs —those most elongated, highly nonlinear lensing features—is sensitive to the matter distribution within the cores of galaxy clusters. The statistics of giant arcs can thus provide useful tests of the structure formation. Cosmological models can be tested by comparing the observed giant arc abundance with the expected abundance from ray-tracing cosmological simulations. In an early study of arc statistics, Bartelmann et al. (1998, hereafter B98) first suggested that the predicted arc abundance by ΛCDM is lower than the observed abundance by approximately an order of magnitude. This order-of-magnitude puzzle has stimulated a significant amount of research toward understanding the most important arc-producing effects. The proposed effects include the triaxiality of cluster mass profiles (Oguri et al. 2003; Dalal et al. 2004; Hennawi et al. 2007; Meneghetti et al. 2010), the amount of intervening large-scale structure (Wambsganss et al. 2005; Hilbert et al. 2007; Puchwein & Hilbert 2009), the rapid increase in the lensing cross section during the major mergers (Torri et al. 2004; Fedeli et al. 2006; Hennawi et al. 2007; Zitrin et al. 2013), the background galaxy redshift distribution (Wambsganss et al. 2004), the cosmological parameters (Bartelmann et al. 2003; Meneghetti et al. 2005; Fedeli et al. 2008; Jullo et al. 2010; D'Aloisio & Natarajan 2011b; Boldrin et al. 2015), the cluster selection criteria (Horesh et al. 2010, 2011), the baryonic mass distribution, primarily in the form of brightest cluster galaxies (BCGs) and substructures (Flores et al. 2000; Meneghetti et al. 2000, 2003, 2010; Hennawi et al. 2007), and the baryon-dragging effects due to cooling (Puchwein et al. 2005; Rozo et al. 2008). Inclusion of these effects has gone a long way toward explaining the "arc statistics problem." However, the tension between the observed arc abundance and the predicted number remained at the level of factor 3, at least for clusters at low redshifts ($z < 0.3$; Horesh et al. 2011). Moreover, a consensus has not yet been reached on which of these physical processes are the dominant ones.

To see whether the remaining discrepancies can be resolved, efforts need to be made on both theoretical and observational fronts. On the theoretical side, all effects that impact arc abundance should be included in the simulations to make them more realistic. A straightforward example is to compare the lensing cross section in simulations with dark and baryonic matter against dark-matter-only simulations (Meneghetti et al. 2003; Puchwein et al. 2005; Killedar et al. 2012). On the observational side, larger, carefully selected cluster samples with ample redshift information are needed. All analyses will also benefit from the utilization of automated procedures for selecting giant arcs as rigorous comparisons must be done using an identical arc selection process for both the actual data and simulated data. In this respect, visual inspection, by which

[11] Hubble Fellow.

early arc statistics studies were conducted, is not an optimal approach as unquantifiable biases can potentially be introduced when classification is done by eye. Several groups have devised tools to search for arcs in an automated manner (Lenzen et al. 2004; Horesh et al. 2005; Alard 2006; Seidel & Bartelmann 2007). Most recently, Horesh et al. (2010, 2011) measured the observed abundance of arcs in a sample of 100 clusters observed with the *Hubble Space Telescope* (*HST*), using an automated and objective arc finder. The observed statistics were compared to those from a simulated data set of cluster images. The simulated images were produced by ray-tracing through a large sample of clusters produced in *N*-body simulations, realistically simulating the observational effects, and then searching for arcs in these simulated clusters using the same arc-finding algorithm. Horesh et al. (2011) found excellent agreement between the observed and simulated arc statistics, particularly for their main subsample of X-ray-selected clusters at redshifts $0.3 < z < 0.6$. However, tension between the observations and simulations remained at other redshift ranges, particularly for the subsample at $z < 0.3$. Moreover, none of the above groups have quantified the performance of their arc finders, such as the arc detection completeness or the false positive rate. Without that information, the arc finders' ability to predict the "true" arc abundance is limited.

In this paper, we measure the observed abundance of giant arcs from the Cluster Lensing And Supernova survey with Hubble (CLASH) sample (Postman et al. 2012). Giant arcs are found in the CLASH images and in simulated images that mimic the CLASH data, using an efficient automated arc-finding algorithm whose selection function has been carefully quantified. CLASH is a 524-orbit multicycle treasury program that targeted 25 massive clusters with $0.18 < z < 0.90$. Twenty of the CLASH clusters are selected based on their X-ray characteristics. The X-ray-selected CLASH sample contains clusters with $T_{\rm x} \geqslant 5\,{\rm keV}$ and with X-ray surface brightness profiles that have low asymmetry. The five remaining clusters were selected based on their expected lensing strength (large Einstein radii, typically $\theta_{\rm Ein} > 30''$ for $z_s = 2$ or high magnification areas). Although the cluster sample is smaller than the one analyzed by Horesh et al. (2010, 2011), the CLASH observations are deeper, and photometric redshift information is available for all arcs brighter than about 26 AB mag (all the magnitudes hereafter are AB mag). In addition, our arc finder is capable of detecting fainter arcs than previous studies. As a result, the total number of arcs that we find is comparable to that in the Horesh et al. studies. We simulate artificial clusters with the same mass and redshift range as the CLASH sample by using the *N*-body simulation-calibrated semianalytic tool MOKA (Giocoli et al. 2012) and directly from the high-resolution, hydrodynamical simulations, MUSIC (Meneghetti et al. 2014), and perform ray-tracing simulation to prepare large sets of realizations for the simulated cluster images. We correct the raw arc counts in both the observations and simulations for incompleteness, false positive detections, and arc elongation measurement bias. This allows us to conduct a direct comparison between the data and the simulations under different theoretical scenarios.

This paper is organized as follows: we describe the arc finder algorithm and its implementation in Section 2 and in the appendices; we demonstrate the arc finder detection efficiency and overall performance in Section 3; we present the arc abundance results for the CLASH observations in Section 4; we describe the cluster simulation and ray-tracing calculations in Section 5; we compare the observed and simulated arc abundance results in Section 6, specifically testing the dependence of the abundance on the source redshift distribution and *c*–*M* relation in Section 7; and a discussion and summary are given in Sections 8 and 9, respectively. Throughout the paper, we adopt a ΛCDM cosmology with parameters $\Omega_m = 0.3$, $\Omega_\Lambda = 0.7$, $\sigma_8 = 0.83$, $H_0 = 100\,h\,{\rm km\,s^{-1}\,Mpc^{-1}}$, and $h = 0.7$ (Planck Collaboration et al. 2014).

2. CONCEPTUAL DEVELOPMENT OF THE ARC FINDER

In early works on arc statistics, arc detection was performed by visual inspection owing, in part, to the complex shapes of arcs and the crowded environments in which they are found. An automated arc-finding algorithm has three key advantages over visual search methods. First, the detection process is reproducible and can be implemented by anyone who learns how to run the code. Second, it can be applied to a large number of real and simulated images. Finally, the detection efficiency and false positive rate can be accurately quantified using artificial objects implanted in real data or using simulated images created by ray-tracing sources through lens models. The biggest challenge to developing such an algorithm is creating a definition of an arc for the purpose of detection that can be implemented in a robust manner using parameters that can be easily quantified from astronomical images.

An ideal arc finder should have the following characteristics:

1. The arc finder should be able to suppress image noise to enhance the contrast of real, low surface brightness arcs without significantly altering the intrinsic shape characteristics of these faint objects.
2. The selection of pixels belonging to arcs should, if possible, not be based on a global fixed intensity threshold as the intensity can vary significantly across a lensed image.
3. The arc finder must employ rules to reject spurious detections such as diffraction spikes from bright stars or edge-on disk galaxies.
4. The arc finder must be able to process many images in a reasonable amount of time.

Here we describe an algorithm for identifying giant arcs—the arcs we are most interested in analyzing in this work. The algorithm was designed to reasonably comply with the above criteria. The parameters that define what we consider to be a giant arc, such as the minimum length and length-to-width ratio, are presented in Section 3.2. Figure 1 shows a flowchart of the steps involved in the algorithm and summarizes its key components. The detailed descriptions of the various steps that compose the algorithm can be found in Appendices A–F.

3. ARC FINDER TESTING AND PERFORMANCE

3.1. Simulating Arcs

To compute the true arc abundance from the detected one, we must quantify the incompleteness and false positive rate of the arc finder using a combination of actual and simulated data sets. The most robust way to simulate arcs is via ray-tracing, in which light rays from objects in a source plane are shot toward

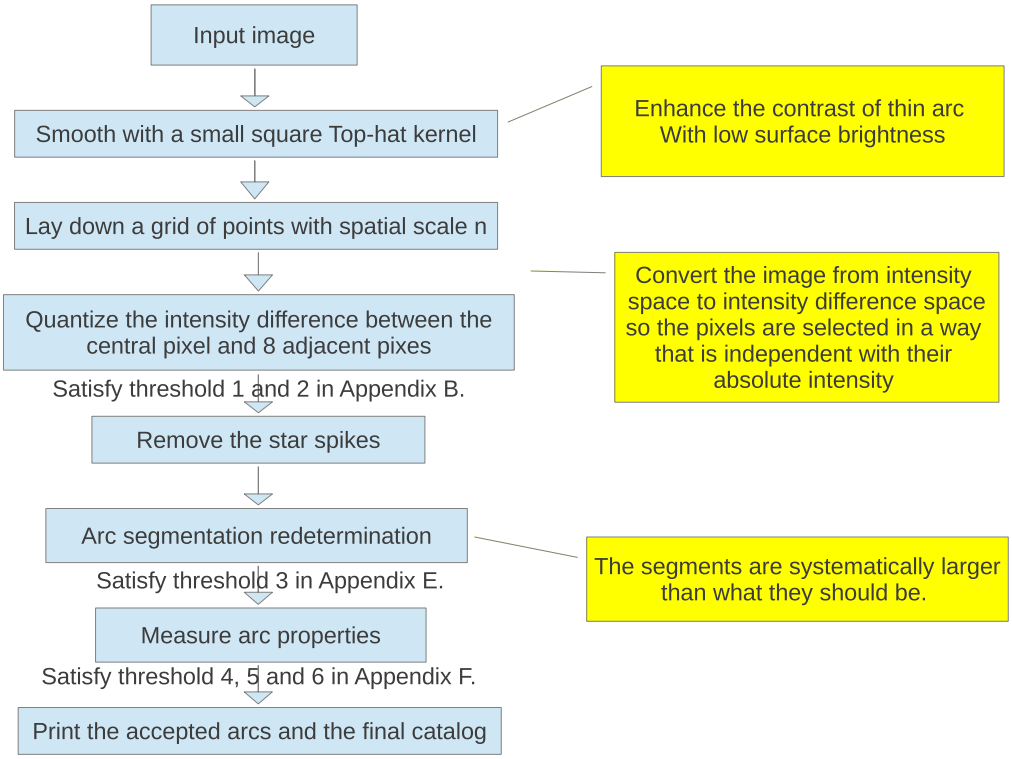

Figure 1. Flowchart of the arc-finding algorithm.

the observer, deflected by the lens plane, and projected onto the image plane (the "sky" as seen by the observer). To quantify the incompleteness and false positive rate, one needs to trace a large number of simulated arcs, which is often very CPU intensive. Moreover, we need full control of all the input parameters of simulated arcs to perform the tests efficiently, and this becomes difficult to do solely by ray-tracing objects that are placed randomly on the source plane.

Furlanetto et al. (2013) use a different approach to simulate the arcs. Their basic idea is to represent an arc as a curved ellipse with its main axis being a segment of a circle. The model arc is then superposed directly on an image at various locations. The arc's shape is set by various parameters (e.g., length, width, curvature, and orientation) chosen to mimic the shapes of real lensed galaxies. The surface brightness distribution is set using a Sérsic law profile. The intensity parameters include the Sérsic index and the intensity at the center of the arc, which allows one to assign any magnitude or the total flux to the simulated arcs. However, this simple analytic prescription does not precisely reproduce the properties of real arcs. For example, the "painted-on" arcs tend to have a deficit of surface brightness at their long ends, which can result in shape measurement biases, especially for faint arcs. For a robust comparison between the real data and simulations, the "painted" arc method falls short of the fidelity that is required.

We adopt a hybrid approach to simulate the arcs: simulate a representative set of arcs via ray-tracing with a range of l/w ratios and surface brightnesses and then "paint" these template arcs onto the background images. This approach keeps the advantages of both methods: realistic arc rendering and fast performance. First, we perform ray-tracing by using a simulated cluster lens with a Navarro–Frenk–White (NFW) profile and a simulated background source with a Sérsic profile. Second, we fine-tune the distance from the source to the caustic line of the lens and carefully measure the l/w ratio of the formed arcs. We keep those arcs with l/w ratio that are closest to integer values as templates, as shown in Figure 2. We then create many additional simulated arcs by arbitrarily rotating the template images and by adjusting the total flux as desired. These arcs are then inserted into both simulated and actual CLASH images for our arc finder performance testing. A detailed discussion on the general detectability of arcs as a function of source properties can be found in Meneghetti et al. (2008).

In order to accurately determine the arc detection completeness, we must account for the effects such as light contamination from cluster galaxies, variable sky background, and instrumental noise. We accomplish this by inserting the arc templates into actual CLASH detection images (a weighted co-addition of all of the Advanced Camera for Surveys [ACS] and WFC3-IR images for a given cluster). An example of a CLASH detection image, with the BCG subtracted out, is shown in Figure 3. We simulate a total of 14,700 arcs spread over seven different l/w values and seven different total flux values. For the purpose of computing a measure of the algorithm's detection completeness, we only look at the fraction of simulated arcs that are detected, even though we are inserting the simulated arcs into real cluster data with real arcs. The completeness is then just the ratio of the number of the simulated arcs detected to the total number of arcs simulated. The inverse of this ratio, $f_{\rm incom} = N_{\rm sim}/N_{\rm det,sim}$, is then the multiplicative factor that we will apply to any raw arc count to correct for incompleteness.

We also utilize the F814W CANDELS (Grogin et al. 2011; Koekemoer et al. 2011) images in the false positive rate test

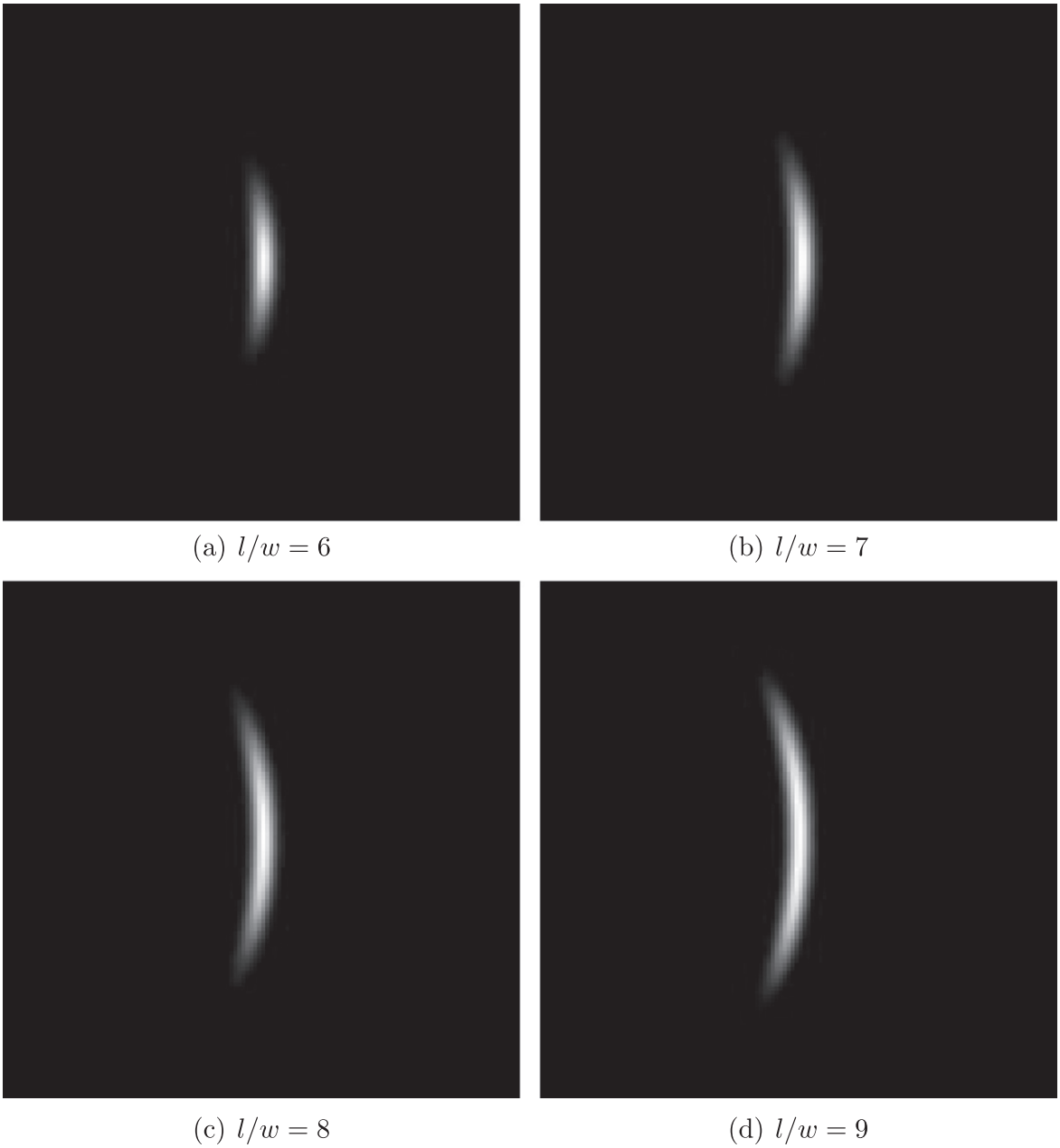

Figure 2. Four arc templates with integer l/w ratios of 6, 7, 8, and 9, respectively, produced by the ray-tracing simulations.

because there are no strong lensed sources in the CANDELS fields. We select images from the CANDELS "Wide programs" (e.g., the UDS and COSMOS fields), which have similar total exposure times to the CLASH detection images (∼50,000 s), and split these mosaics into smaller images that match the angular size of the CLASH co-added images. We run the arc finder on the CANDELS data and compute the surface density of detections as functions of both the l/w threshold and the total arc length, l. This constitutes the basis for our false positive correction function.

We use the CLASH data with simulated arcs to measure our arc finder completeness as a function of arc length, l/w ratio, and arc signal-to-noise ratio (S/N). Here we define the S/N of the arc as $\sum I_i \Big/ \sqrt{\sum(\sigma^2_{i,\mathrm{bn}} + I_i)}$, where I_i is the intensity from the source at pixel i and $\sigma^2_{i,\mathrm{bn}}$ is the combined variance due to the sky background and all sources of detector noise at pixel i. In our completeness test, the total flux of each drawn arc is adjusted to match the assigned S/N value. We use the CANDELS images to assess the arc finder false positive rate. Figure 4 shows the completeness versus the l/w detection threshold, $(l/w)_{\mathrm{thr}}$, at S/N = 3 and 10. The completeness remains at a high level (>80% for S/N = 10) when $l/w \geqslant (l/w)_{\mathrm{thr}}$; Figure 5(a) shows the false positive rate in the CANDELS data as a function the l/w detection threshold when the minimum arc length is set to $2''$. The detected number of false positives is slightly above 10 arcmin^{-2} at low $(l/w)_{\mathrm{thr}}$, while it decreases rapidly as $(l/w)_{\mathrm{thr}}$ increases. Figure 5(b) shows the false positive rate as a function of the length of the objects when the l/w threshold is set to 7. The number of false positive detections peaks in the length bin $5'' \leqslant l < 6''$. The spurious detections can thus be suppressed if we adopt a minumum length threshold of $l \geqslant 6''$.

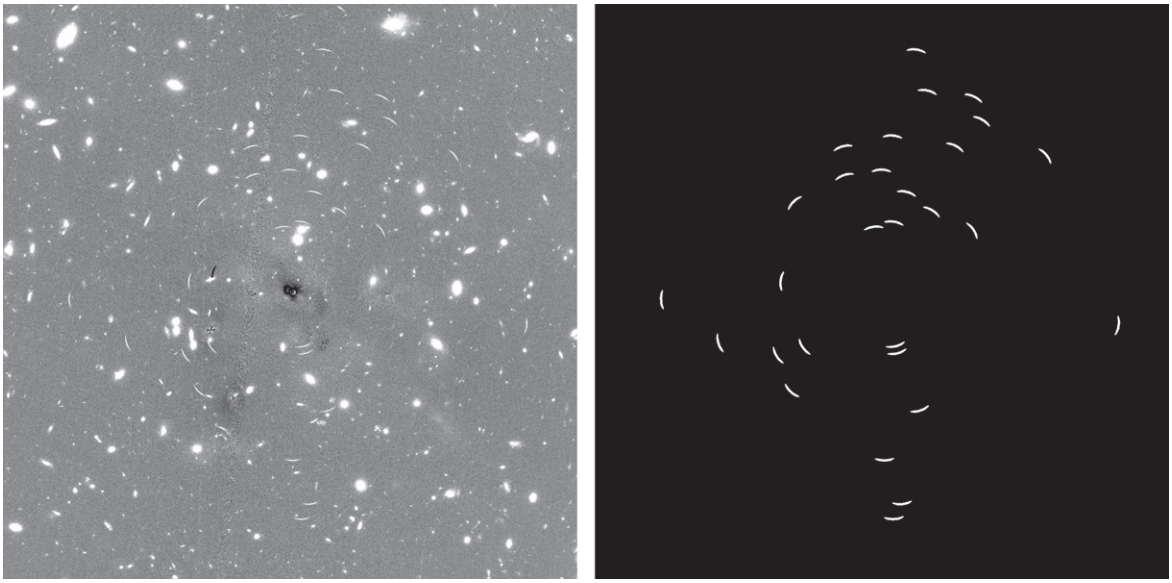

(a) Simulated arcs (b) Detected arcs

Figure 3. (a) CLASH detection image for Abell 1423 shown with 30 "painted" arcs with $l/w = 7$. The BCG and a handful of its satellites are first subtracted off before the arc finder is run. (b) The arcs that are detected are shown. The field of view of both images is $2\farcm7 \times 2\farcm7$.

We have not applied this minimum length threshold to our completeness test because the identification of the arcs does not depend on the length (only depends on l/w and S/N). Moreover, the intensity gradient along the ridge line of the arc should be smaller than that in the perpendicular direction, which means that the length measurement should be more immune to the noise effects. To test that, we measure the ratio of the detected length to the true length of the simulated arcs. Figure 6(a) shows the distribution of the ratio at three different S/N levels. The dashed lines indicate the median value of the ratio. We can see that both the distribution and the median value remain statistically similar at different S/N levels.

3.2. Determination of the Optimal l/w Detection Threshold

In previous studies, the l/w detection threshold is typically set to 7.5, 8, or 10. Generally, the reason to set a high l/w threshold is to avoid the inclusion of highly elliptical and edge-on spiral galaxies into the arc sample. In general, the lower l/w threshold one uses, the more contamination one gets. Hence, it is desirable to find an l/w threshold that maximizes the completeness level and minimizes the false positive rate. We now use our measured estimates of the completeness and false positive rate as a function of the minimal l/w to identify the optimal l/w threshold to use in the construction of our final arc catalog. We do this by identifying the smallest l/w threshold at which the surface density of detected simulated arcs, $N_{\rm det}$, exceeds the surface density of false positive detections, $N_{\rm fpr}$, by a factor of 5 or more. The results of this test are shown in Figure 6(b). We find that the ratio $N_{\rm det}(\geqslant(l/w)_{\rm thr})/N_{\rm fpr}(\geqslant(l/w)_{\rm thr})$ is always larger than 5 when the l/w detection threshold is larger than 7. We thus adopt the l/w detection threshold of 7 in our analysis of the arc abundance. The false positive rate for $l/w \geqslant 7$ and an arc length threshold $l \geqslant 6''$ is 1.5 ± 0.4 arcmin^{-2}. We use this false positive rate to correct our corresponding raw arc counts.

3.3. l/w Elongation Bias, Incompleteness, and False Positive Rate Correction

There are three statistical corrections we need to apply to the raw counts of the giant arcs. First, the detected l/w is not equal to the true l/w. The background noise and/or the segmentation boundaries of a detected object may systematically affect the determination of the l/w ratio. We need to determine how the detected l/w ratio deviates from the true l/w ratio at different S/N levels and correct for this elongation bias in a statistical sense. For example, as shown in Figure 7, the detected l/w ratio of arcs can be biased high by image noise, as the noise tends to make arcs appear thinner than they actually are. Second, we need to apply the incompleteness correction (presented above) as there will always be some real arcs that are missed by our detection algorithm. Third, we need to apply a false positive correction as there are always some objects misidentified by the arc-finding algorithm. We apply all these three corrections in deriving the final observed and simulated arc abundances.

To compute the l/w elongation bias correction, we collect all the detected arcs with measured $l/w \geqslant 6.5$,[12] and we assign them to one of three bins: $6.5 \leqslant l/w < 7.5$, $7.5 \leqslant l/w < 8.5$, and $l/w \geqslant 8.5$. We also assign their corresponding true l/w ratios to one of three bins: $l/w = 7$, $l/w = 8$, and $l/w \geqslant 9$. We further split each bin into three sub-bins by their S/Ns: $S/N < 5$, $5 \leqslant S/N < 10$,and $S/N \geqslant 10$. We then calculate the mean value and standard deviation of the correction factor for the elongation bias $f_{\rm bias} = N_{\rm true}/N_{\rm det}$, where $N_{\rm true}$ and $N_{\rm det}$ are the number of simulated arcs and detected arcs in each bin, respectively.

[12] In practice, we set the l/w threshold to be 6.5 instead of 7. The bias correction is then done by comparing the arcs with detected ratios in the range $6.5 \leqslant l/w < 7.5$ to the number with true $l/w = 7$.

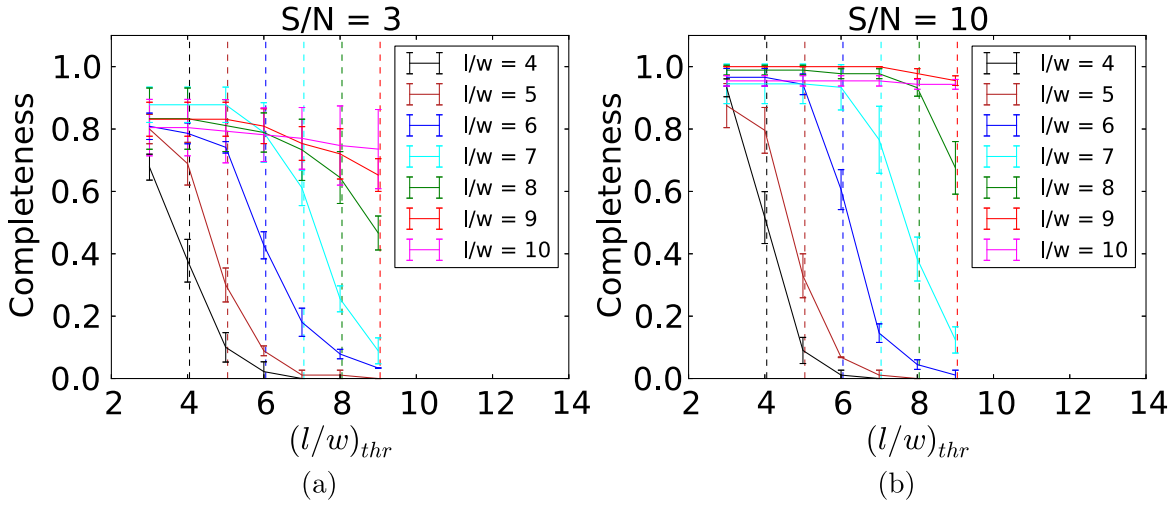

Figure 4. Completeness as a function of the l/w threshold for seven different true l/w ratios at (a) S/N = 3 and (b) S/N = 10. The dashed lines indicate $l/w = (l/w)_{\rm thr}$, and the error bars denote the 1σ rms error.

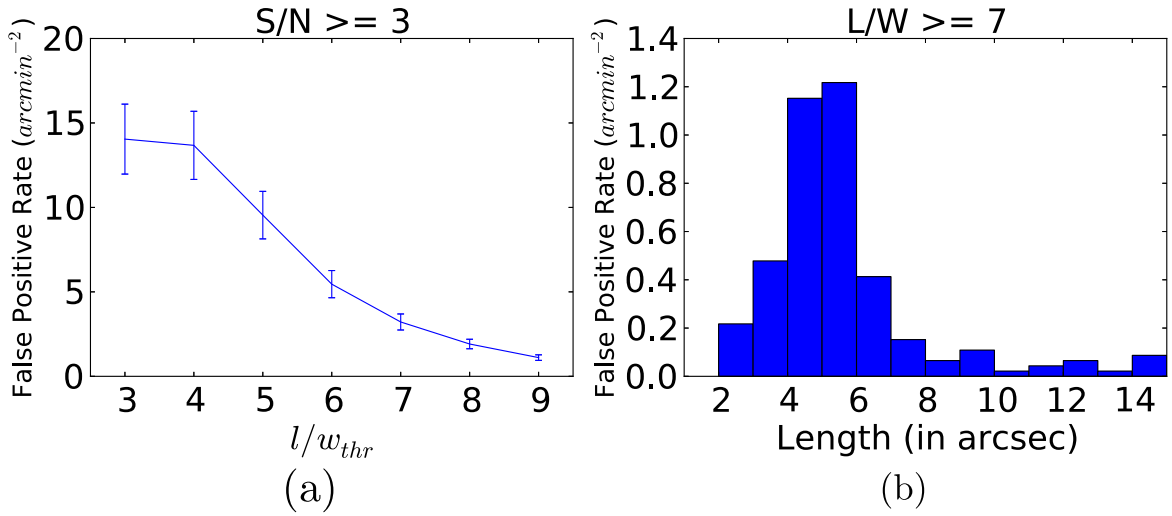

Figure 5. (a) False positive rate per unit area as a function of the detected l/w threshold for arcs with S/N $\geqslant$ 3. (b) False positive rate per unit area as a function of the arc length for arcs with $l/w \geqslant 7$. Results are based on running the arc finder on CANDELS data. The error bars denote the 1σ rms error.

The true arc count, $N_{\rm true}$, is then computed as follows:

$$N_{\rm true} = \sum_i N_{{\rm det},i} \times f_{{\rm bias},i} \times f_{{\rm incom},i} - N_{\rm false}$$

$$\sigma_{\rm true} = \sqrt{N_{\rm true} \times \sum_i \left[\left(\frac{\sigma_{{\rm bias},i}}{f_{{\rm bias},i}} \right)^2 + \left(\frac{\sigma_{{\rm incom},i}}{f_{{\rm incom},i}} \right)^2 \right] + \sigma^2_{\rm false}}, \quad (1)$$

where $N_{{\rm det},i}$ is the observed number of arcs in each bin and i goes over all the bins. As shown in Figures 8(a) and (b), most of the measured l/w are biased high, especially for the arcs with intrinsically low l/w. The completeness remains above 80% for all the cases. Here, biased high means that arcs with "true" low l/w have their l/w values systematically overestimated. The mean ratio of the observed l/w to the "true" l/w also appears to be dependent on the true l/w ratio, as shown in Figure 7.

3.4. Comparison of Arc Finder's Performance with a Previous Code

We compare the arc detection efficiency of our arc finder with that of the only publicly available arc-finding code from Horesh et al. (2005). We simulate a large amount of arc with different l/w ratios and draw Gaussian random noise onto the arcs to produce simulated arc images with seven different S/N levels. We run both arc-finding algorithms on these simulated data sets.

Figure 9 shows the detection rate versus the arc S/N level for arcs with true $l/w = 7$, 10, at a detection threshold $l/w \geqslant 7$. We have computed the S/N for detected arcs found using each of the algorithms using the definition given in Section 3.1. For the bright arcs (S/N > 10), the detection rates for both arc finders remain high (>90%); for faint arcs ($5 \leqslant$ S/N < 10), the Horesh et al. (2005) arc finder's detection rate drops rapidly, while our algorithm's detection efficiency remains higher than 90%; for very faint arcs (S/N < 5), our detection

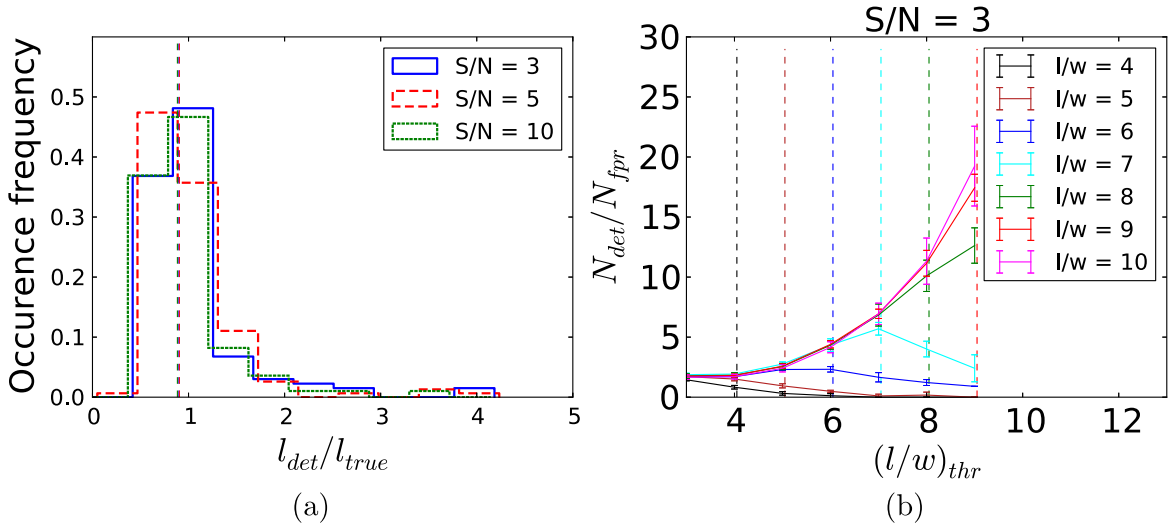

Figure 6. (a) Distribution of the ratio of the detected length to the true length at three different S/N levels. The colored dashed lines denote the median values of the distribution. (b) Ratio of the number of detections per unit area to the false positive rate per unit area as a function of the detected l/w threshold. The dashed lines indicate $l/w = (l/w)_{\rm thr}$, and the error bars denote the 1σ rms error.

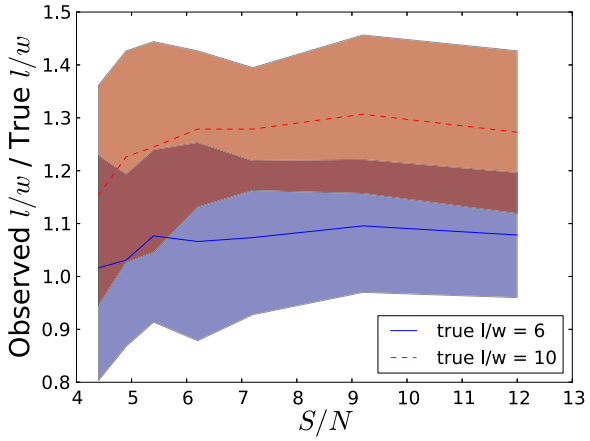

Figure 7. Ratio of the observed l/w to true l/w as a function of the arc S/N. The height of the shaded regions denotes the 1σ rms errors on the ratio.

rate drops to about 80%. The advantage of our intensity-gradient-based arc-finding algorithm is nicely demonstrated in Figure 9, especially for the detection of large arcs with low surface brightness.

4. ANALYSES OF THE CLASH DATA

4.1. Arc Statistics for the CLASH Sample

The CLASH observations for each cluster consist of 16 broadband images (spanning the range 0.23μ–1.6μ) using the WFC3/UVIS, WFC3/IR, and ACS/WFC instruments on board *HST*. The cluster properties are listed in Table 1. We run our arc finder on the detection (ACS + WFC3/IR) image created for each cluster. We detect a raw total of 187 arcs with $l/w \geqslant 6.5$ in 20 X-ray-selected CLASH clusters. After applying our minimum arc length criterion $l \geqslant 6''$, the arc count drops to 81 giant arcs selected from the 20 X-ray-selected CLASH clusters. Correcting for the elongation bias and incompleteness brings the total number of detected arcs in 20 X-ray-selected clusters to 104 ± 12. After further correcting for the false positive rate, we find a lensing efficiency of 4 ± 1 arcs per X-ray-selected cluster. Throughout this paper, the lensing efficiency denotes the number of arcs per cluster. There are 28 arcs with $l/w \geqslant 6.5$ and $l \geqslant 6''$ detected in the five high-magnification CLASH clusters, corresponding to a mean value of 5 ± 1 arcs per cluster after all corrections are applied. Figure 10 shows the distributions of number of arcs per cluster for the X-ray-selected cluster sample and the high-magnification cluster sample. Figure 11 shows the comparison of the detection images with the raw output of the arc finder with $l/w > 7$ for five CLASH clusters.

4.2. The Arc Redshift Distribution

We determine the photometric redshift distribution of the lensed background galaxies detected by our algorithm using the photometric redshifts derived with the Bayesian-based BPZ package (Benítez 2000; Benítez et al. 2004; Coe et al. 2006). Spectral energy distribution (SED) templates are redshifted and fitted to the observed photometry. The BPZ code adopts a prior that the empirical likelihood of redshift is a function of both galaxy magnitude and galaxy morphological type (e.g., bright and/or elliptical galaxies are rare at high redshift). We used 11 SED templates originally from PEGASE (Fioc & Rocca-Volmerange 1997) that have been recalibrated based on photometry and spectroscopic redshifts of galaxies in the FIREWORKS catalog (Wuyts et al. 2008). We obtain the photometric redshift distribution of all the detected arcs and find that they have a median photometric redshift $z_s = 1.9$. We also find that there is a significant fraction of arcs with $z_s \sim 3$ (34% of the detected arcs have photometric redshift larger than 3). Figure 12 shows the arc number counts as a function of redshift before and after correcting for the measurement bias, incompleteness, and false positive rate. To compute the photometric redshift distribution of our arc sample, we sum up the individual posterior redshift probability distributions of each detected arc. The mean uncertainty of the photometric redshifts in CLASH is $\sigma_z \sim 0.03(1+z)$, and thus we sample the probability distribution using the bin size $\Delta z = 0.4$, which is twice as large as the uncertainty of the arc with the highest redshift. The summed distribution prior to correction for our selection function and elongation bias is shown as the blue line

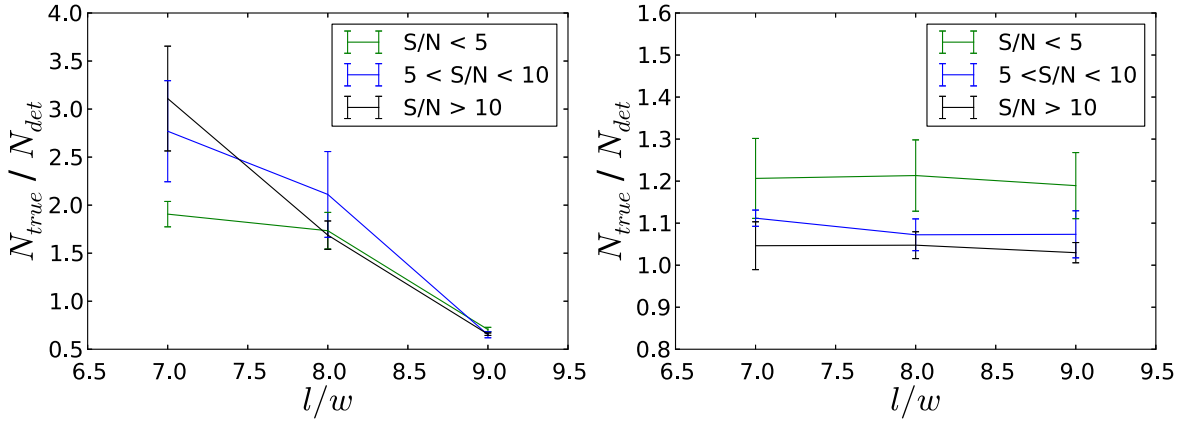

(a) Elongation bias correction (b) Incompleteness correction

Figure 8. All the detected arcs with $l/w \geqslant 6.5$ are assigned to three l/w bins (horizontal axis). (a) Elongation bias correction factors in three l/w bins. (b) Incompleteness correction factors in three l/w bins. The error bars denotes the 1σ rms error.

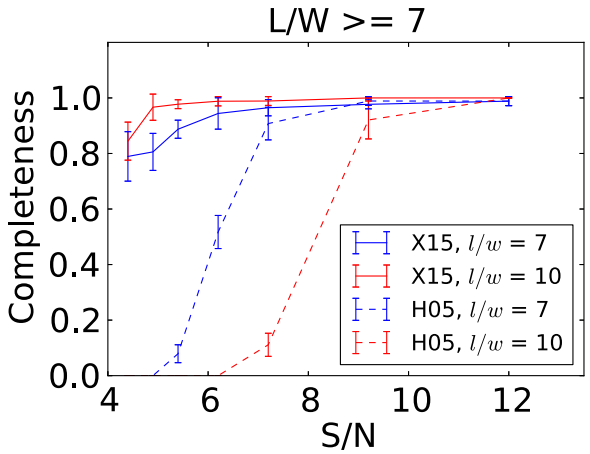

Figure 9. Comparison of the arc detection completeness between our arc finder (solid curves) and the Horesh et al. (2005) arc finder (dashed curves) for arcs with $l/w = 7$, 10. The error bars denote the scatter. For bright arcs with S/N > 10 both arc finders maintain a high detection rate (>90%), while for faint arcs with lower S/N levels, our arc finder exhibits considerably higher detection efficiency. The error bar denotes the 1σ rms error.

in Figure 12. To correct for the selection bias, incompleteness, and false positive rate, we re-sum the probability distribution for each arc after first multiplying by the appropriate correction factors. The fully corrected redshift distribution, derived in this way, is shown by the red line in Figure 12. Figure 13 also lists the distribution of arc S/N, arc AB magnitude in the F814W filter, arc l/w ratio, and the normalized angular distance of the arc from the cluster center. Table 2 lists the properties of all the detected arcs in the sample of 20 X-ray-selected clusters, including the equatorial and pixel coordinates, length, l/w ratio, radial distance from the arc center to the cluster center, the normalized radial distance by r_{200}, the photometric redshift, and the AB magnitude in the F814W band. In Table 2, we do not exclude the objects with photometric redshifts that are significantly smaller than the corresponding cluster redshift. Such probable foreground sources are considered to be false positive detections. We eliminate false positive detections statistically when we calculate the arc redshift distribution in the CLASH sample.

5. MOKA LENSING SIMULATIONS

5.1. The MOKA-simulated Cluster Sample

In order to confirm or resolve the arc statistics problem, we require realistic model predictions to compare with the observed CLASH arc counts. In previous studies, mock clusters were selected from *N*-body simulations using either dark matter only (Wambsganss et al. 2004; Hilbert et al. 2007; Horesh et al. 2010) or dark matter with other ingredients (Puchwein et al. 2005; Gottlöber & Yepes 2007; Hilbert et al. 2008; Rozo et al. 2008; Meneghetti et al. 2010). The simulated clusters were then projected onto the plane of the sky as viewed from various directions to create the 2D mass models. However, the total number of clusters and/or their mass and redshift ranges used in these prior studies are not optimally matched to the CLASH data set. Therefore, we generate a simulated cluster sample by running the publicly available MOKA package (Giocoli et al. 2012). MOKA uses simulation-calibrated analytical relations to describe the dark matter and baryonic content of clusters, which allows one to incorporate all the cluster properties that are relevant for strong cluster lensing. For example, for each halo, a triaxial NFW profile and a random orientation are assigned. The axial ratios are generated from the prescriptions of Jing & Suto (2002). The halo concentration, c, and its dependence on cluster mass, M, and redshift are modeled based on the c–M relation of Bhattacharya et al. (2013) The joint weak-lensing + strong-lensing analysis by Merten et al. (2015) and Umetsu et al. (2014) indicates that the observed c–M relation derived from the 20 X-ray-selected CLASH clusters agrees with the relation presented in Bhattacharya et al. (2013). The scatter in the concentration value at a fixed mass is well described by a Gaussian distribution instead of a lognormal distribution, with rms ~ 0.33. We adopt this scatter in our MOKA simulations. The dark matter substructures, the central BCG, and adiabatic contraction are also incorporated into the MOKA-generated models. MOKA is computationally efficient and is able to create a single simulated cluster lens model in a few CPU seconds on a personal computer by using a fast semianalytic approach. The details of the code and its implementation can be found in Giocoli et al. (2012).

Table 1
The CLASH Cluster Sample

Cluster[a]	α_{J2000}	δ_{J2000}	z_{Clus}	M_{200c} $[10^{15}\,M_{\odot}\,h^{-1}]$
X-Ray-selected Clusters				
Abell 209	01:31:52.57	−13:36:38.8	0.206	0.95 ± 0.07
Abell 383	02:48:03.36	−03:31:44.7	0.187	0.87 ± 0.07
MACS 0329.7–0211	03:29:41.68	−02:11:47.7	0.450	0.73 ± 0.10
MACS 0429.6–0253	04:29:36.10	−02:53:08.0	0.399	0.80 ± 0.14
MACS 0744.9+3927	07:44:52.80	+39:27:24.4	0.686	0.70 ± 0.04
Abell 611	08:00:56.83	+36:03:24.1	0.288	0.85 ± 0.05
MACS 1115.9+0129	11:15:52.05	+01:29:56.6	0.352	0.90 ± 0.09
Abell 1423	11:57:17.26	+33:36:37.4	0.213	...
MACS 1206.2–0847	12:06:12.28	−08:48:02.4	0.440	0.86 ± 0.11
CLJ 1226.9+3332	12:26:58.37	+33:32:47.4	0.890	1.56 ± 0.10
MACS 1311.0–0310	13:11:01.67	−03:10:39.5	0.494	0.46 ± 0.03
RXJ 1347.5–1145	13:47:30.59	−11:45:10.1	0.451	1.16 ± 0.19
MACS 1423.8+2404	14:23:47.76	+24:04:40.5	0.545	0.57 ± 0.10
RXJ 1532.9+3021	15:32:53.78	+30:20:58.7	0.345	0.53 ± 0.08
MACS 1720.3+3536	17:20:16.95	+35:36:23.6	0.391	0.75 ± 0.08
Abell 2261	17:22:27.25	+32:07:58.6	0.224	1.42 ± 0.17
MACS 1931.8–2635	19:31:49.66	−26:34:34.0	0.352	0.69 ± 0.05
RXJ 2129.7+0005	21:29:39.94	+00:05:18.8	0.234	0.61 ± 0.06
MS 2137–2353	21:40:15.18	−23:39:40.7	0.313	1.04 ± 0.06
RXJ 2248.7–4431 (Abell 1063S)	22:48:44.29	−44:31:48.4	0.348	1.16 ± 0.12
High-magnification Clusters				
MACS 0416.1–2403	04:16:09.39	−24:04:03.9	0.420	...
MACS 0647.8+7015	06:47:50.03	+70:14:49.7	0.584	...
MACS 0717.5+3745	07:17:31.65	+37:45:18.5	0.548	...
MACS 1149.6+2223	11:49:35.86	+22:23:55.0	0.544	...
MACS 2129.4–0741	21:29:26.06[a]	−07:41:28.8[a]	0.570	...

Note.
[a] Central cluster coordinates derived from optical image.

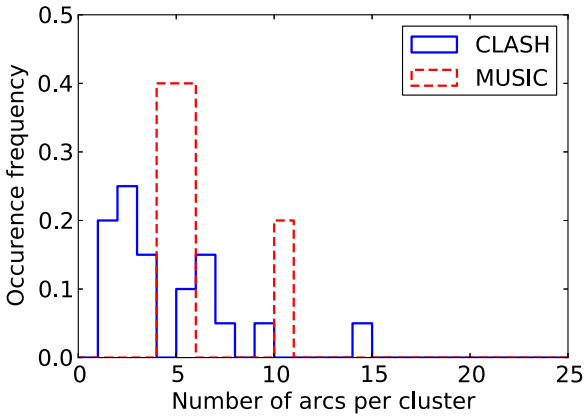

Figure 10. Occurrence frequency of arcs per cluster for 20 X-ray-selected CLASH clusters (blue) and for the subsample of five high lens magnification CLASH clusters (red).

For our study, we create 640 mock clusters with the same mass and redshift range as the 20 X-ray-selected CLASH clusters (32 different realizations for each corresponding mass and redshift). In particular, the density profile of the main halo follows an NFW profile, while the density profile of the subhalos is chosen to be a truncated singular isothermal sphere profile; the spatial density distribution of the subhalos follows the measurement from numerical simulations by Gao et al. (2004); the mass resolution of the subhalos is $10^{10}\,M_{\odot}$. We calculate the deflection angle, convergence, and shear fields for each projected mass distribution. The angular resolution of the simulated cluster images is $0\farcs065$, which matches the pixel scale in the CLASH images.

5.2. Background Source Images and Ray-tracing Method

To create the sky scene from the MOKA mass models, we follow a methodology similar to that in Horesh et al. (2011): we choose galaxies from the F775W UDF image as the sample of sources to be lensed by our simulated cluster mass models. This ensures that we have a realistic background field that incorporates the observed distributions of galaxy morphologies, redshifts, luminosities, angular sizes, and ellipticities directly into our simulation. We then simulate the lensed UDF images via ray-tracing, as briefly described in Section 3.1. Adopting the thin lens approximation, the lensing can be described by the lens equation,

$$\beta = \theta - \alpha(\theta, z_s), \tag{2}$$

where θ is the image position, β is the source position in the source plane, and α is the deflection angle, which has a weak dependence on source redshift. Coe et al. (2006) have produced a UDF photometric redshift catalog and a corresponding segmentation map containing 9821 objects detected

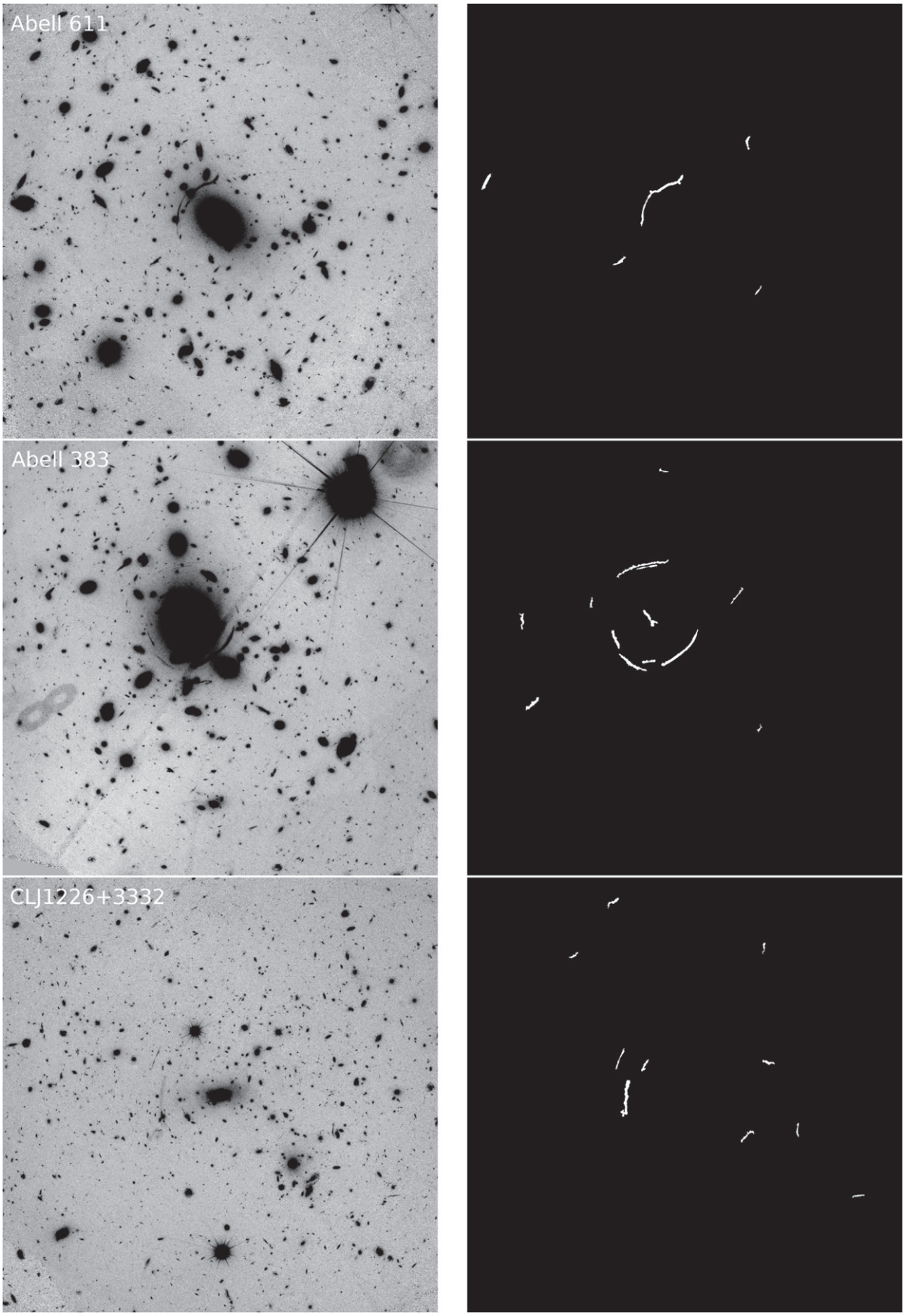

Figure 11. Left: detection images of five CLASH clusters; right: raw output maps produced by the arc finder with $l/w > 7$.

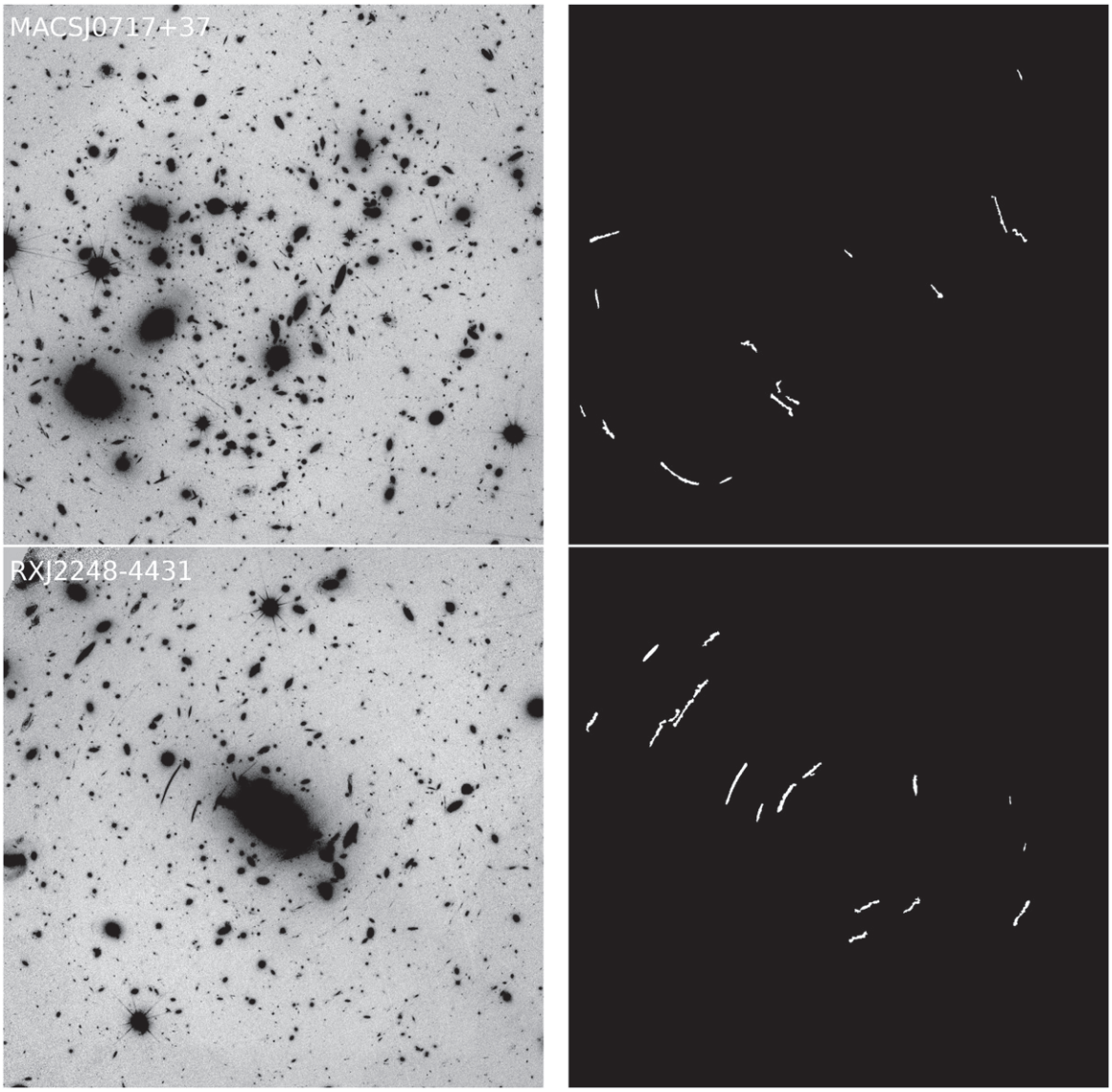

Figure 11. (Continued.)

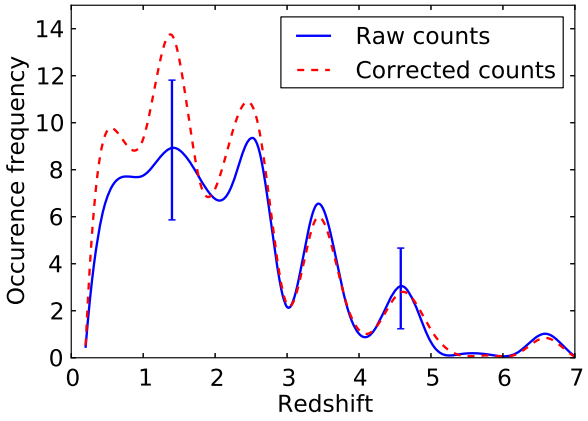

Figure 12. Photometric redshift distribution of the detected arcs in the CLASH X-ray-selected sample. The blue solid line denotes the redshift distribution of the raw data counts, which is computed based on the full posterior probability distribution of the detected arcs; the red dashed line denotes the redshift distribution after the elongation bias, incompleteness, and false positive correction, which is computed based on the corrected full posterior probability distribution. The error bar represents the 1σ Poisson error.

above an 8σ level. Based on the redshift catalog, we assign all the UDF sources among 20 redshift bins with bin widths of $\Delta z = 0.3$. In each redshift bin (α is then fixed) we perform the ray-tracing to generate the simulated lensed image and combine each of the simulated lensed objects from all bins into a final image. Finally, we match the noise levels in the simulations to that in the CLASH images.

6. COMPARISON BETWEEN SIMULATED IMAGES AND REAL OBSERVATIONS

We run the arc finder on all 640 simulated images. A raw total of 3304 arcs with $l/w \geqslant 6.5$ and $l \geqslant 6''$ are detected in 640 simulated realizations. We correct this total number of arcs for elongation bias and incompleteness and obtain 3585 ± 165 arcs, giving a mean of 4 ± 1 arcs per cluster after applying the false positive correction. This value matches the observed lensing efficiency of 4 ± 1 precisely. There is no significant difference between the arc abundance detected in the observations and that detected in the MOKA simulations.

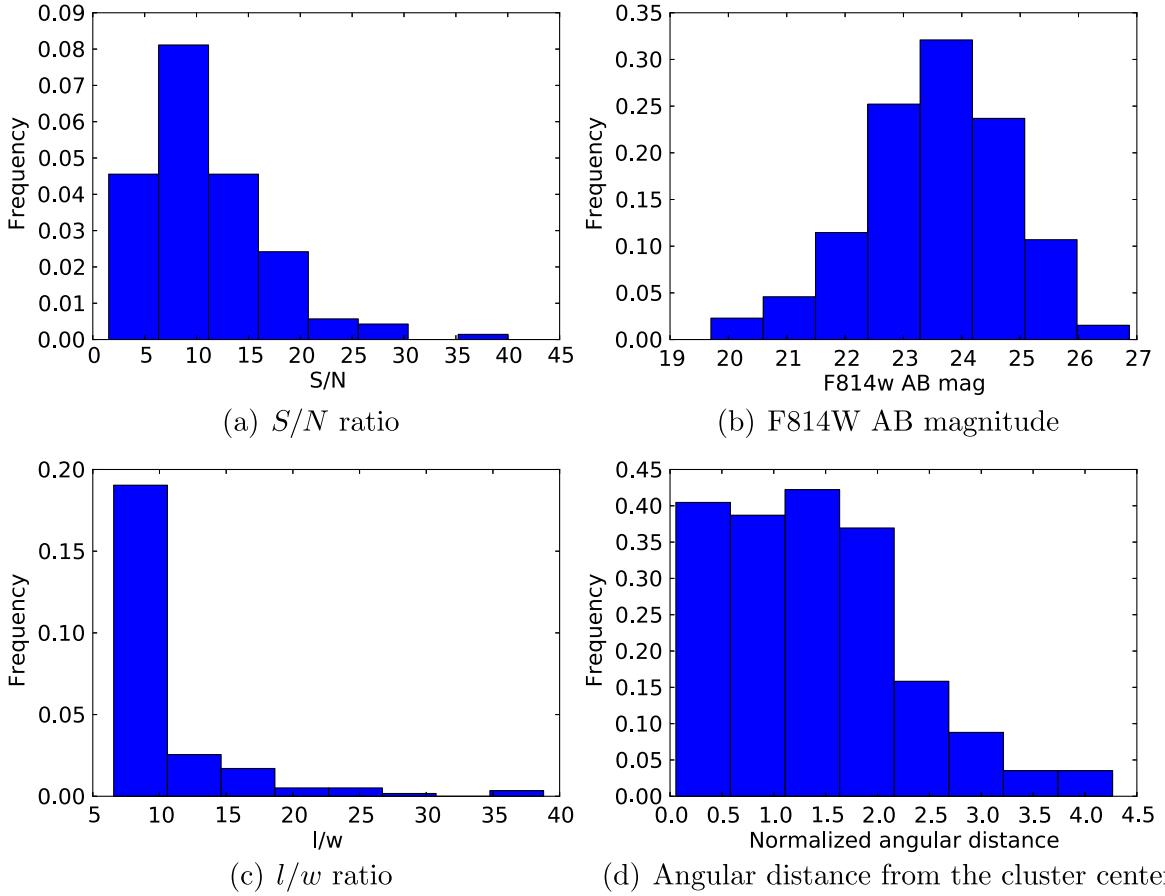

Figure 13. Distribution of (a) S/N, (b) AB magnitude, (c) l/w ratio, and (d) normalized angular distance RD/r_{200} of all the detected arcs in the CLASH sample.

Examining the observed and simulated distribution of number of arcs per cluster (Figure 14), a Kolmogorov–Smirnov (K-S) test[13] yields a p-value $= 0.92$, indicating that the null hypothesis that both distributions are drawn from the same parent distribution cannot be strongly rejected. We further test the lensing efficiency as a function of cluster redshift by dividing the observed and simulated samples into two subsamples by their redshift: $z_{\rm CL} \leqslant z_{\rm median}$ and $z_{\rm CL} > z_{\rm median}$, where $z_{\rm median} = 0.352$. For each subsample, we compare the observed and simulated number distribution (see Figure 15) of the lensing efficiency. On average, the higher-redshift clusters are slightly more efficient lenses than the lower-redshift clusters, but the differences are all at marginal statistical significance. The K-S test indicates that, in both redshift bins, the observed and simulated distributions of the lensing efficiency are consistent with being drawn from a common population (p-values are 0.99 and 0.65 for the lower- and higher-redshift bins, respectively). We summarize our arc statistics results for the observations and simulations in Table 3. The second and third columns in Table 3 denote the lensing efficiency of the observed and simulated samples, respectively; the fourth column is the p-value of the K-S test on the observed and simulated distributions.

We now explore the relationships between the lensing efficiency and the cluster's redshift, mass, concentration, and effective Einstein radius $\theta_{E,\rm eff} = \sqrt{A/\pi}$ for CLASH and MOKA samples, where A is the area enclosed by the tangential critical curve. Figure 16 shows the lensing efficiencies as functions of cluster redshift, mass, central concentration, and $\theta_{E,\rm eff}$. Since the CLASH sample does not span a very wide range in the cluster redshift, mass, and concentration, it is perhaps not surprising that there are no clear correlations between the lensing efficiency and the redshift, the mass, or the concentration for both the CLASH and MOKA samples. However, there is a very significant correlation between the MOKA lensing efficiency and $\theta_{E,\rm eff}$, and the correlation can be described by the following formula:

$$N_{\rm arc} = (0.03 \pm 0.01)\theta_{E,\rm eff}^{1.54\pm0.08}[\rm arcsec] + (0.81 \pm 0.22), \quad (3)$$

as the dashed line in Figure 16(d) shows. The nonzero value of the y-intercept reflects a contribution from false positive detections (consistent with our estimation from simulations) and intrinsic scatter.

7. WHAT IS THE DOMINANT DETERMINANT OF CLUSTER LENSING EFFICIENCY?

We now assess the relative importance of the redshift distribution of the lensed sources and the c–M relation of the clusters on the resulting giant arc abundance. We accomplish this by conducting a series of simulations where we alter either the redshift distribution of the background galaxies or the assumed c–M relation. While other effects such as dark matter substructure, halo triaxiality, and the mass profile of the BCG may also play a role in determining the distribution of arc

[13] The K-S test performed here uses the `ks_2samp` routine from the SciPy package.

Table 2
Detected Arcs and Properties

Cluster	Arc ID	R.A.	Decl.	x	y	l ($''$)	l/w	RD ($''$)[a]	RD/r_{200}	z	AB mag (F814W)
Abell 1423	1	179.33	33.60	2204.00	1905.00	6.82	9.67	43.09	1.09	0.62	22.61
⋯	†2	179.30	33.62	3553.00	3227.00	6.14	7.61	82.69	2.10	0.00	24.29
Abell 209	1	22.96	−13.61	2760.00	2738.00	11.90	10.00	23.16	0.62	3.50	21.73
Abell 2261	†1	260.59	32.12	3542.00	1698.00	7.08	8.89	84.98	1.84	0.00	24.39
⋯	†2	260.61	32.12	2505.00	1994.00	8.46	10.55	32.18	0.70	0.33	23.01
⋯	3	260.62	32.13	2165.00	2317.00	6.72	7.92	24.54	0.53	3.54	23.75
⋯	4	260.60	32.13	2902.00	2395.00	10.55	14.29	26.77	0.58	1.80	22.07
⋯	†5	260.64	32.13	1324.00	2620.00	13.06	23.34	76.98	1.67	0.27	23.79
⋯	6	260.61	32.15	2577.00	3516.00	6.64	10.20	66.94	1.45	1.35	23.22
Abell 383	1	42.03	−3.54	1620.00	2246.00	6.80	7.03	54.43	1.30	0.73	25.74
⋯	2	42.02	−3.53	2181.00	2462.00	12.36	14.63	17.70	0.42	4.22	22.94
⋯	3	42.01	−3.53	2553.00	2616.00	19.23	22.41	15.27	0.36	0.89	20.15
⋯	4	42.02	−3.53	2114.00	2579.00	7.32	7.91	15.79	0.38	3.12	23.20
⋯	5	42.03	−3.53	1566.00	2735.00	6.33	8.56	49.75	1.18	2.46	25.06
⋯	†6	42.01	−3.53	2314.00	2691.00	8.43	9.01	1.04	0.02	0.30	21.93
⋯	7	42.00	−3.53	2828.00	2893.00	7.48	17.11	34.96	0.83	6.31	23.92
⋯	8	42.01	−3.52	2281.00	3035.00	20.42	31.37	22.65	0.54	5.00	23.33
⋯	9	42.01	−3.52	2281.00	3024.00	7.87	16.59	21.94	0.52	3.24	24.81
Abell 611	1	120.24	36.06	2335.00	2665.00	25.66	30.64	15.35	0.40	1.12	20.44
⋯	†2	120.26	36.06	1358.00	2727.00	7.02	7.37	75.89	2.00	0.27	19.75
CLJ 1226	1	186.74	33.54	2838.00	2253.00	6.30	9.52	26.72	1.52	2.79	25.90
⋯	2	186.75	33.54	2164.00	2394.00	14.22	12.37	23.10	1.31	2.30	24.96
⋯	3	186.75	33.55	2144.00	2742.00	8.47	19.19	28.47	1.62	3.45	23.79
MACS 0329	1	52.41	−2.19	3049.00	2869.00	7.96	9.55	43.27	1.56	1.03	23.28
⋯	2	52.42	−2.18	2685.00	3153.00	6.20	9.45	44.66	1.61	3.35	24.25
MACS 0429	1	67.40	−2.90	2752.00	1709.00	6.48	8.01	52.93	2.08	1.67	24.22
⋯	2	67.40	−2.89	2499.00	2200.00	10.69	12.24	18.83	0.74	1.35	21.79
MACS 0744	†1	116.22	39.44	2682.00	1488.00	7.00	7.56	66.12	3.43	0.41	20.22
⋯	2	116.23	39.45	2128.00	2078.00	6.41	7.74	36.39	1.89	4.79	23.85
⋯	†3	116.20	39.45	3147.00	2191.00	7.32	7.32	45.92	2.38	0.14	18.48
⋯	4	116.23	39.46	1969.00	2581.00	6.75	9.40	35.47	1.84	4.73	23.99
⋯	5	116.23	39.46	2033.00	2625.00	6.10	8.37	32.04	1.66	4.41	24.43
⋯	6	116.20	39.46	3477.00	2652.00	7.56	14.86	63.92	3.32	4.11	23.76
⋯	7	116.21	39.46	2839.00	2632.00	6.77	7.71	23.47	1.22	1.17	20.34
MACS 1115	1	168.96	1.49	2602.00	2228.00	14.44	18.05	18.34	0.58	2.46	23.08
⋯	2	168.98	1.50	1586.00	2402.00	9.53	15.25	60.03	1.90	1.76	24.83
⋯	†3	168.97	1.50	2500.00	2374.00	7.76	7.60	7.74	0.25	0.42	20.91
⋯	4	168.97	1.50	2355.00	2371.00	10.65	12.58	12.57	0.40	4.21	21.72
⋯	5	168.96	1.51	2896.00	2911.00	14.52	16.16	37.20	1.18	4.12	22.91
⋯	6	168.96	1.51	2578.00	3022.00	7.14	7.11	34.71	1.10	3.25	24.41
MACS 1206	†1	181.55	−8.81	2247.00	2078.00	6.69	7.04	28.16	0.99	0.55	20.26
⋯	2	181.54	−8.80	2790.00	2454.00	14.27	15.73	19.47	0.68	1.05	19.76
⋯	3	181.54	−8.80	3292.00	2420.00	6.54	7.51	52.08	1.83	2.41	24.64
⋯	†4	181.55	−8.80	2477.00	2438.00	11.97	10.88	0.92	0.03	0.49	23.77
⋯	5	181.57	−8.80	1618.00	2471.00	8.39	12.32	56.79	1.99	1.56	23.19
⋯	6	181.53	−8.79	3484.00	3134.00	8.36	8.57	78.90	2.77	0.72	19.30
MACS 1311	1	197.75	−3.17	2881.00	2742.00	6.25	7.66	29.33	1.30	2.83	24.77
MACS 1423	†1	215.93	24.07	3433.00	2050.00	9.84	17.73	66.78	3.12	0.00	23.74
⋯	2	215.95	24.07	2606.00	2128.00	6.13	7.80	24.49	1.14	1.47	23.92
⋯	3	215.94	24.07	2804.00	2120.00	8.80	15.30	30.97	1.45	2.57	23.94
⋯	4	215.95	24.08	2378.00	2773.00	8.18	11.48	20.10	0.94	1.79	22.72
⋯	5	215.95	24.09	2576.00	3211.00	7.70	11.46	47.03	2.20	3.16	24.47
MACS 1720	1	260.06	35.60	2757.00	2042.00	8.33	11.23	33.32	1.20	4.38	24.29
⋯	2	260.07	35.60	2621.00	2346.00	8.60	10.80	11.90	0.43	0.82	23.23
MACS 1931	1	292.96	−26.59	2559.00	1917.00	9.71	11.49	37.90	1.38	3.55	24.23
MS 2137	1	325.06	−23.66	2422.00	2713.00	14.81	12.99	14.59	0.46	1.77	21.78
⋯	2	325.07	−23.65	2181.00	2903.00	10.75	14.08	33.37	1.05	1.71	23.95
⋯	3	325.07	−23.65	2215.00	3046.00	10.93	12.95	39.93	1.26	1.97	23.86
RXJ 1347	1	206.87	−11.77	3032.00	1776.00	12.76	21.51	55.55	1.82	1.64	23.58
⋯	2	206.87	−11.76	3141.00	2064.00	9.07	11.79	46.58	1.52	2.43	21.57
⋯	3	206.87	−11.75	3117.00	2872.00	7.02	10.12	43.42	1.42	4.28	24.63
⋯	4	206.88	−11.75	2521.00	2951.00	6.82	7.51	29.92	0.98	0.78	21.46
⋯	5	206.88	−11.74	2549.00	3162.00	7.83	13.50	43.50	1.42	3.78	24.22
RXJ 1532	†1	233.22	30.34	2841.00	2088.00	7.75	9.30	34.16	1.25	0.27	22.25

Table 2
(Continued)

Cluster	Arc ID	R.A.	Decl.	x	y	l (″)	l/w	RD (″)[a]	RD/r_{200}	z	AB mag (F814W)
RXJ 2129	1	322.41	0.08	2890.00	2044.00	7.42	7.79	38.34	1.36	3.17	23.61
⋯	†2	322.44	0.09	1394.00	2310.00	6.26	9.57	73.09	2.60	0.00	24.96
⋯	3	322.42	0.09	2295.00	2528.00	7.20	7.83	13.81	0.49	1.55	22.65
RXJ 2248	1	342.18	−44.54	2613.00	1950.00	6.15	6.89	36.42	1.31	3.08	24.18
⋯	2	342.16	−44.54	3371.00	2095.00	8.91	11.34	62.35	2.25	3.09	24.02
⋯	3	342.18	−44.54	2622.00	2084.00	8.06	10.83	28.10	1.01	1.64	23.35
⋯	4	342.17	−44.54	2830.00	2074.00	6.61	9.53	34.94	1.26	2.75	24.42
⋯	5	342.19	−44.53	2227.00	2545.00	10.12	10.26	18.06	0.65	1.41	22.36
⋯	6	342.19	−44.53	2039.00	2697.00	13.95	17.47	32.67	1.18	1.38	21.32
⋯	7	342.17	−44.53	2853.00	2642.00	6.19	7.28	24.70	0.89	1.41	22.35
⋯	8	342.19	−44.53	2343.00	2684.00	7.32	8.80	15.81	0.57	3.76	24.48
⋯	9	342.20	−44.52	1664.00	2902.00	9.44	13.06	60.38	2.18	1.36	25.23
⋯	†10	342.21	−44.52	1358.00	2943.00	6.42	7.33	79.70	2.87	0.00	21.79
⋯	11	342.20	−44.52	1743.00	2930.00	10.16	14.05	56.68	2.04	2.79	24.33
⋯	12	342.20	−44.52	1856.00	3108.00	6.95	7.97	57.66	2.08	1.96	24.89
⋯	†13	342.21	−44.52	1629.00	3261.00	6.73	6.85	75.27	2.71	0.40	19.07
⋯	14	342.20	−44.52	1909.00	3340.00	6.49	7.68	66.85	2.41	0.85	24.11

Note.
[a] RD = radial distance from the arc center to the cluster center in units of arcseconds; IDs with † denote the false positive detection.

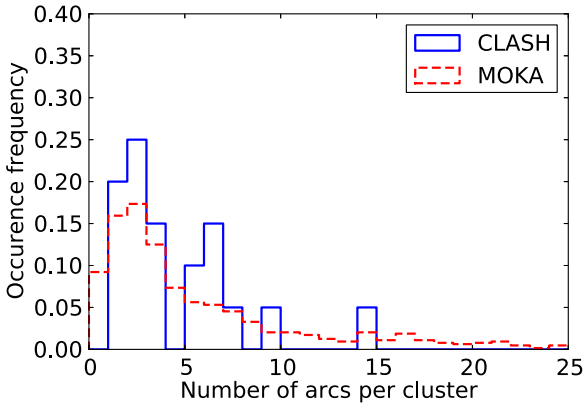

Figure 14. Comparison of distribution of arc number per cluster between the X-ray-selected CLASH sample and the MOKA-simulated sample with the same mass and redshift range.

number counts, we focus here on studying the impact of the redshift distribution and c–M relation as these are potentially the most important effects. As shown below, however, we find that the lensing efficiency of CLASH-like clusters is not very sensitive to the redshift distribution of the background galaxy population so long as there is a significant fraction of the source galaxy population that lies at $z > 1$. We also find that the lensing efficiency is quite sensitive to the dark matter concentration distribution.

7.1. Simulated Lenses, Background Sources All at $z_s = 1$ or $z_s = 2$

We start by testing how the source redshift distribution affects the arc abundance. We use the same 160 simulated MOKA clusters but we first set all the UDF source redshifts to $z_s = 1$ and then, in a separate realization, set all source redshifts to $z_s = 2$ to see the impact of a delta function redshift distribution (which is obviously an extreme assumption). We then perform the ray-tracing to create 640 new simulated images for each case. We run the arc finder on these images and detect 1748 and 3764 arcs in total, respectively, when $z_s = 1$ and $z_s = 2$. After applying statistical corrections, we find lensing efficiencies of 2 ± 1 ($z_s = 1$) and 5 ± 1 ($z_s = 2$). The lensing efficiency decreases by a factor of about 2 when the background redshift distribution is a delta function with all sources at $z_s = 1$. However, when putting all sources at $z_s = 2$, one obtains a similar lensing efficiency to that obtained when using a realistic UDF redshift distribution. The distributions of arc number per cluster for these three cases are shown in Figure 17(a). K-S tests indicate that the arc number distributions when using the UDF redshift distribution and using a delta function at $z_s = 2$ are consistent (p-value = 0.45). The arc number distribution when assuming a $z_s = 1$ delta function differs significantly from that with a UDF redshift distribution or $z_s = 2$ delta function redshift distribution (K-S test p-value $= 3.5 \times 10^{-6}$).

7.2. CLASH Mass Models (CLMM), UDF Redshift Distribution for the Background Galaxies

Given the CLMM, we would like to check whether the UDF field is representative as a background source for the simulations. We use the publicly available mass models of 19 CLASH X-ray-selected clusters (Zitrin et al. 2015) to lens the UDF source galaxies and to create 152 simulated images. We detect 656 arcs from these images, corresponding to a lensing efficiency of 3 ± 1. This efficiency differs from that found for the actual CLASH images (4 ± 1) by 0.7σ. The distributions of arc number per cluster are consistent with one another (see Figure 17(b)). A K-S test gives a p-value = 0.42.

7.3. CLMM, Background Sources All at $z_s = 1$ or $z_s = 2$

We now assess whether the lensing efficiency is altered significantly when using the CLMM along with delta function redshift distributions. Again, we arbitrarily place all the UDF sources at redshift $z_s = 1$ and $z_s = 2$ and perform ray-tracing through 19 CLASH mass models to create 152 new simulated images for each case. We detect a total of 414 and 670 arcs for the $z_s = 1$ and $z_s = 2$ source distributions, respectively. These

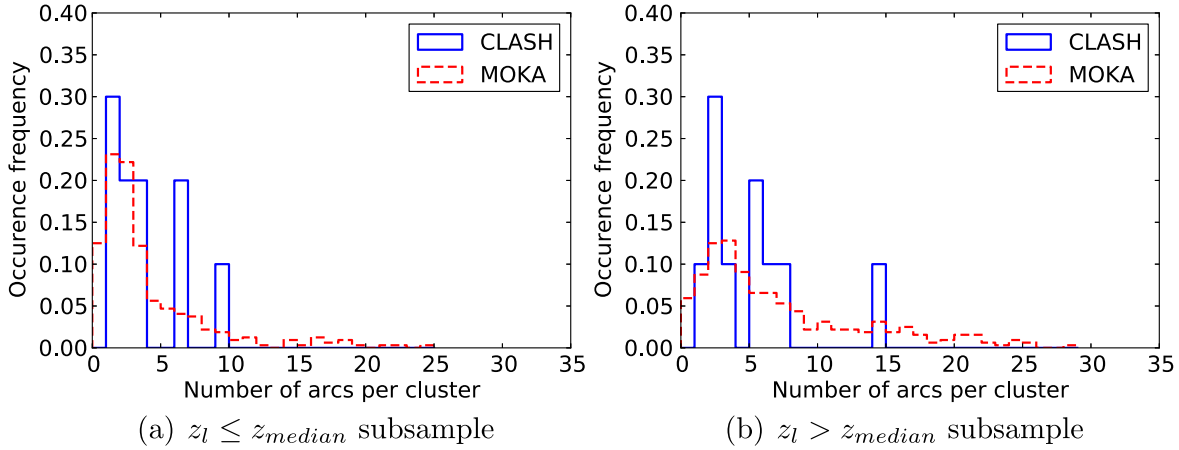

Figure 15. Lensing efficiency as a function of cluster redshift. The 20 X-ray-selected CLASH clusters are divided into two subsamples by their cluster redshift: $z_{\rm CL} \leqslant z_{\rm median}$ and $z_{\rm CL} > z_{\rm median}$, where $z_{\rm median} = 0.352$. (a) and (b) list the comparison of the number distribution of the subsamples between the observation and simulation.

Table 3
Comparison of Observed and Simulated Cluster Lensing Efficiencies

Redshift Range	CLASH Observations	MOKA Simulations	p-value of K-S Test
All Clusters	4 ± 1	4 ± 1	0.92
$z_{\rm CL} \leqslant z_{\rm median}$	3 ± 1	3 ± 1	0.99
$z_{\rm CL} > z_{\rm median}$	5 ± 1	6 ± 1	0.65

correspond to lensing efficiencies of 2 ± 1 and 3 ± 1. Similar to those in the MOKA simulations, the lensing efficiency and distribution of arc numbers are similar for simulations with UDF redshift distribution and $z_s = 2$ (p-value $= 0.5$), whereas the lensing efficiency for $z_s = 1$ is again about 2 times lower than that with a UDF redshift distribution and $z_s = 2$, and the arc number distribution for $z_s = 1$ is also significantly different (K-S p-value $= 1.8 \times 10^{-4}$). Figure 17(c) shows the distributions of arc number per cluster for the three samples.

7.4. Different c–M Relations, UDF Redshift Distribution for the Background Galaxies

Here we show how the arc abundance depends on the cluster c–M relation. Using the UDF redshift distribution, we re-simulate 160 new clusters and simulated images with MOKA by adopting the c–M relation in Neto et al. (2007), instead of Bhattacharya et al. (2013). We detect 230 arcs from 160 realizations using the Neto et al. (2007) c–M relation, which, after corrections, yields a lensing efficiency of 1 ± 1. The lensing efficiency is a factor of 4 lower using the Neto et al. (2007) c–M relation than when we adopt the Bhattacharya et al. (2013) c–M relation. This arc abundance is seen to be quite sensitive to the parameters of the c–M relation. As above, Figure 17(d) shows the arc number distributions of three samples.

8. MUSIC LENSING SIMULATIONS

Although the lensing efficiency in semianalytic MOKA simulations is in excellent agreement with that found in the CLASH observations, it is important to make sure that this is a robust result. Thus, we study a different suite of simulations to determine the arc abundance using simulated clusters drawn directly from high-resolution, hydrodynamical simulations. For this, we use a set of mock clusters taken from the MUSIC-2 N-body/hydrodynamical simulations (Meneghetti et al. 2014). The MUSIC-2 sample (Sembolini et al. 2013; Biffi et al. 2014) consists of a mass-limited sample of re-simulated halos selected from the MultiDark cosmological simulation. This simulation is dark matter only and contains 2048^3 particles in a $(1\,h^{-1}$ Gpc$)^3$ cube, which was performed in 2010 using ART (Kravtsov et al. 1997) at the NASA Ames Research Center. All these simulations are accessible from the online MultiDark Database2. The run was using the best-fitting cosmological parameters to WMAP7+BAO+SNI ($\Omega_M = 0.27$, $\Omega_b = 0.0469$, $\Omega_\Lambda = 0.73$, $\sigma_8 = 0.82$, $n = 0.95$, $h = 0.7$). There were 282 cluster-scale halos in the simulation box that are more massive than $10^{15}\,h^{-1}\,M_\odot$ at redshift $z = 0$ and are selected to construct our sample. All these massive clusters were re-simulated both with and without radiative physics. The initial conditions for the re-simulations were generated in a finer mesh of size 4096^3, by following the zooming technique described in Klypin et al. (2001). By doing so, the mass resolution of the re-simulated objects corresponds to $m_{\rm DM} = 9.01 \times 10^8\,h^{-1}\,M_\odot$ and to $m_{\rm SPH} = 1.9 \times 10^8\,h^{-1}M_\odot$, which was improved by a factor of 8 with respect to the original simulations. The parallel TREEPM+SPH GADGET code (Springel 2005) was used to run all the re-simulations. Snapshots for 15 different redshifts in the range $0 \leqslant z \leqslant 9$ are stored for each re-simulated object. The snapshots that overlap with the redshifts of the CLASH clusters are at $z = 0.250$, 0.333, 0.429, and 0.667.

These re-simulated cluster halos were originally used to estimate the expected concentration–mass (c–M) relation for the CLASH cluster sample (Meneghetti et al. 2014; Merten et al. 2015). As in these works, we use the X-ray image simulator X-MAS (Gardini et al. 2004) to produce simulated *Chandra* observations of the halos, and we use them to further identify objects that match the X-ray morphologies and masses of the X-ray-selected CLASH clusters. The c–M relation from our X-ray-selected set of simulated clusters agrees with that directly derived from the CLASH data at the 90% confidence level (Merten et al. 2015) and is fully consistent with the stacked weak-lensing signal derived from the ground-based wide-field observations (Umetsu et al. 2014). We perform ray-tracing through these X-ray-selected simulated clusters (BCGs and radiative physics are not included) to lens the UDF sources and create 100 simulated CLASH images.

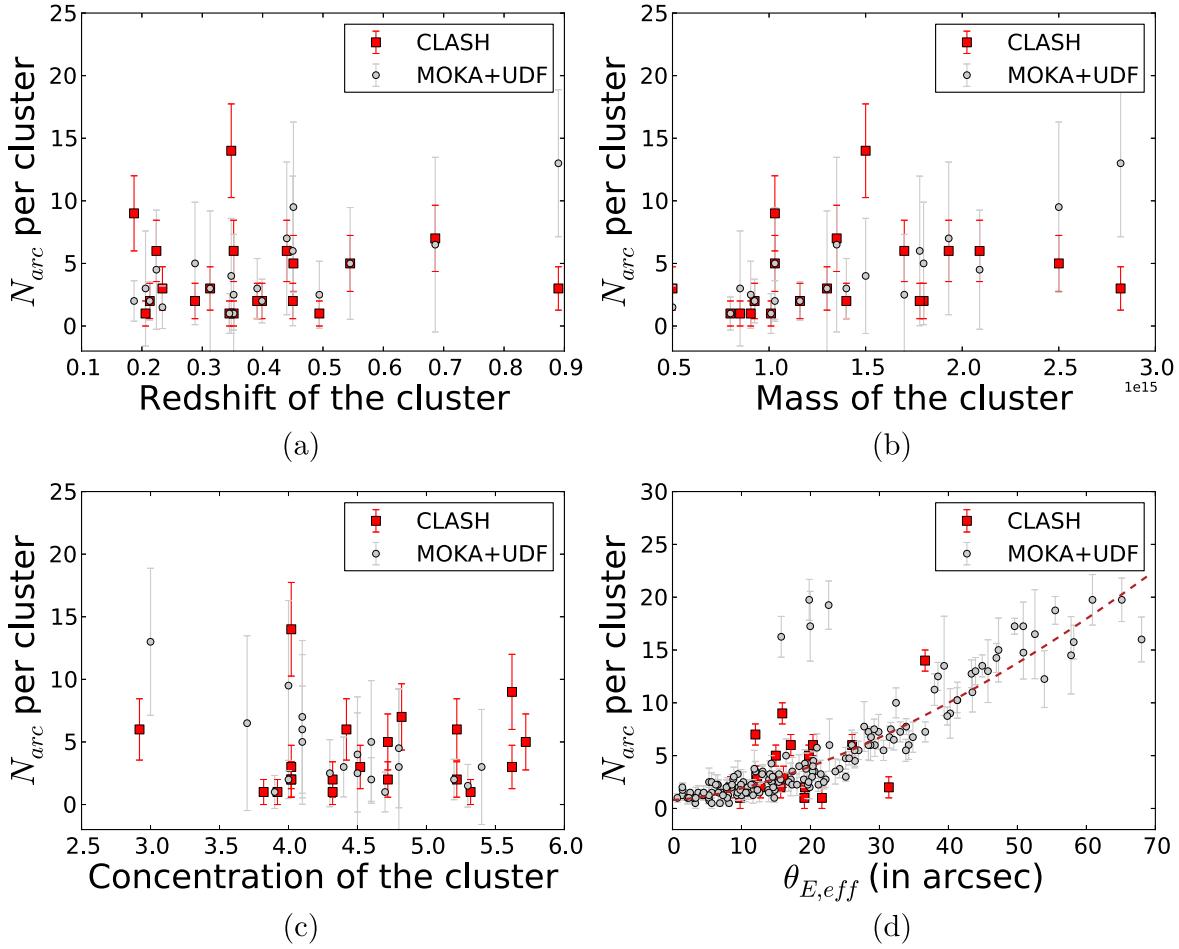

Figure 16. Comparisons of the lensing efficiency between the CLASH and MOKA samples for (a) the corresponding cluster redshift, (b) mass, and (c) concentration. (d) Relation between the lensing efficiency and the effective Einstein radius $\theta_{E,\mathrm{eff}}$ for all the CLASH and MOKA data points. With the upper left outlier excluded, the dashed line gives the best-fitting curve for all the MOKA data points.

8.1. Lensing Statistics of MUSIC-simulated Samples and Comparison with Real Observations

We run the arc finder on the 100 MUSIC-simulated images and detect a total of 343 arcs with $l/w \geqslant 7$ and $l \geqslant 6''$. We correct the total number of arcs for the elongation bias and incompleteness, yielding a final number of 447 ± 24 arcs, which corresponds to a mean value of 3 ± 1 arcs per cluster after application of the false positive correction. The MUSIC lensing efficiency is fully consistent with the lensing efficiency of the observed CLASH X-ray-selected sample (4 ± 1). Figure 18(a) shows the observed and simulated distributions of arc number per cluster. A K-S test between these two distributions has a p-value $= 0.95$. We also explored the dependence of the lensing efficiency on the l/w_{min} and l_{min} in the MUSIC simulations (Figures 18(b), (c)). The lensing efficiency decreases with increasing l/w_{min} and l_{min} values, which is consistent with the behavior seen in the CLASH observations. We summarize the main arc statistics results of this paper in Table 4: the second column in Table 4 is the rounded-off value of the mean lensing efficiency (number of arcs per cluster); the third column is the significance of difference in lensing efficiency between the specific simulation sample and that derived for the observed CLASH X-ray-selected sample. As with the MOKA simulations, the MUSIC-simulated clusters yield cluster lensing efficiencies that match that seen in the observations when the simulations adopt a *c–M* relationship and a source redshift distribution that matches the observations.

9. DISCUSSION

Since the arc statistics was originally proposed as a cosmological probe, many previous studies have investigated the sensitivity of the arc abundance on various cosmological effects. Cosmology enters the strong-lensing properties of the galaxy clusters in two ways: first, the arc abundance depends on the angular-diameter distance and volume, which are determined by the cosmological expansion; second, the arc abundance depends on the cluster abundance and internal structure, which are cosmological sensitive. *N*-body simulations and semianalytic approaches have been utilized in earlier studies to explore the sensitivity of arc abundance on σ_8 (Wambsganss et al. 2004; Li et al. 2006; Fedeli et al. 2008), and an increaseing function of arc abundance with σ_8 has been observed, though whether the large increments in arc abundance when increasing the σ_8 are quantitatively reliable is not clear. Boldrin et al. (2015) have studied the arc abundance dependence on σ_8 and Ω_m for a given survey area. They use MOKA to generate mock clusters with different mass and redshift and populate them into the light cones spanned by the survey region. They identify the increasing functions of arc

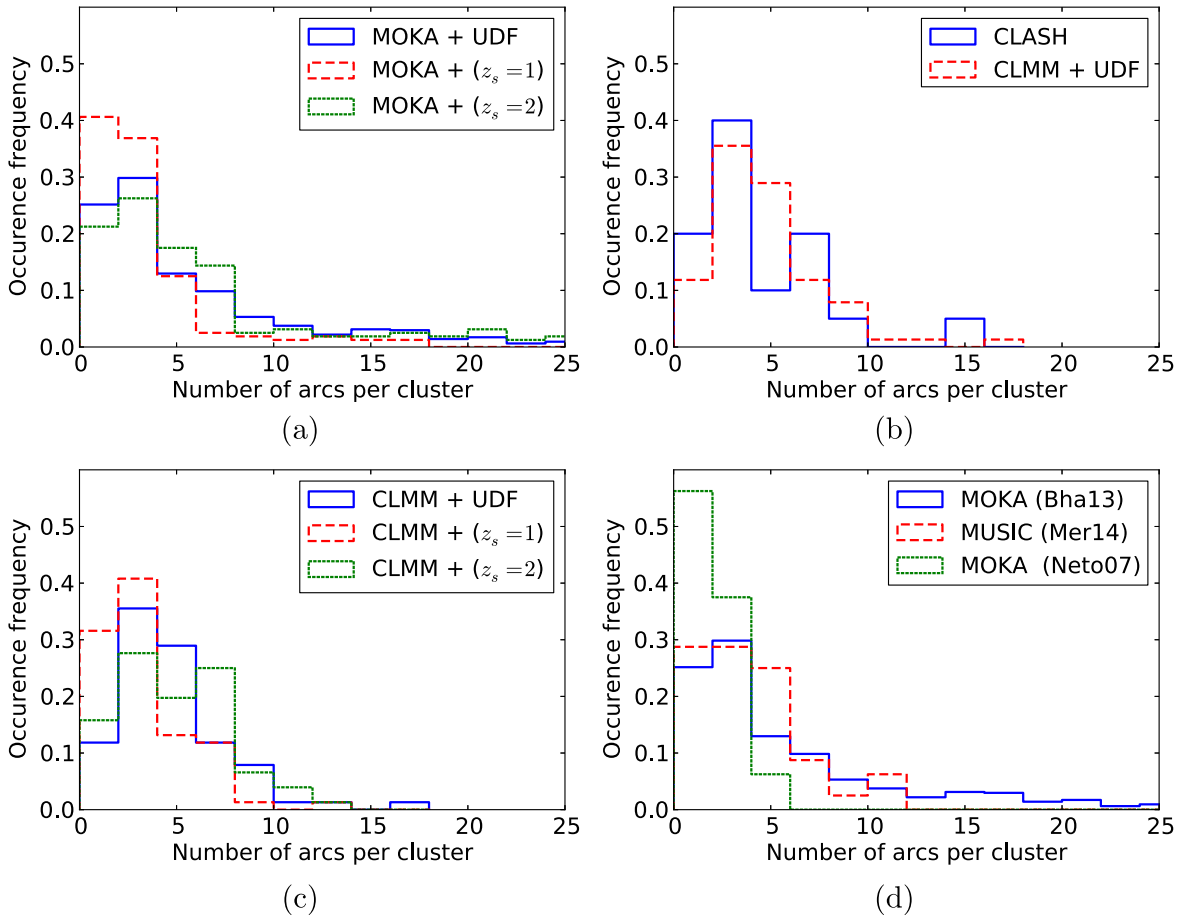

Figure 17. Comparison of the distribution of arc number per cluster between diffrent samples. (a) Comparison of the arc number distribution between samples with MOKA mass models and different source redshift distributions; (b) comparison of the arc number distribution between the CLASH sample and CLMMs (CLASH mass models) using the UDF redshift distribution; (c) comparison of the arc number distribution between samples with CLMMs and different source redshift distributions; (d) comparison of the arc number distribution between samples with the same source redshift distributions and mass models, but implemented with different c–M relations.

abundance with both parameters. The arc abundance seems more sensitive to σ_8 than Ω_m, because σ_8 has an effect on the cluster formation time, which in turn affects the cluster internal lensing properties such as triaxiality and concentration. However, the degeneracy between two parameters for the arc abundance limits its ability to distinguish different cosmologies. The arc abundance sensitivity on various dark energy models has also been studied, which includes a constant equation-of-state parameter $w \neq 1$ (Bartelmann et al. 2003) and time-varying w parameter (Meneghetti et al. 2005); the arc abundance could change by at most a factor of 2 even with a substantial change in w. Jullo et al. (2010) and D'Aloisio & Natarajan (2011b) studied how cosmology affects the arc statistics through geometry effects. They found the expansion function; thus, the cosmological models can be constrained from the ratio of the lensing efficiencies at different redshifts. To achieve competitive results, however, the mass distribution of the clusters must be determined with very high precision, and a sample of about 10 clusters contaning about 20 arc families each is needed. Moreover, the arc statistics could even change by 30% with different non-Gaussianity parameters based on a theoretical framework (D'Aloisio & Natarajan 2011a). Therefore, these studies may indicate that, among all the cosmological parameters, the arc abundance seems to be most sensitive to σ_8. Interestingly, most of the simulations in early arc statistics works have adoped a typically higher σ_8 value ($\sim$0.9–0.95; $\sigma_8 = 1.12$ was adopted in B98) than the current concensus from *WMAP7* and *Planck*, which could have made the discrepancy between the simulations and the observations even larger. It implies that at least the deficit of cluster abundance under different cosmologies might not be the main solution to the "arc statistics problem" in the first place. Since the dependence of the cluster internal lensing properties on σ_8 is still not well known, we simply adopt the value of $\sigma_8 = 0.83$ along with other cosmological parameters from the *Planck* results (Planck Collaboration et al. 2014). We believe that our conclusion would not change significantly unless there is large revision in the the *Planck* value for σ_8.

As one of the promising candidate solutions to the arc statistics problem, the impact of source redshift distribution on the arc abundance has been emphasized by many previous studies. Wambsganss et al. (2004) studied the magnification probability for light rays propagating across a cosmological scale and found that the probability of high-magnification events highly depends on the source redshift. They concluded that the arc abundance should have a steep increase with source redshift because the number of halos suitable for strong lensing increases exponentially with redshift, and they suggest this as the solution for the arc statistics problem. Bayliss et al. (2011) and Bayliss (2012) have established a large sample of arcs

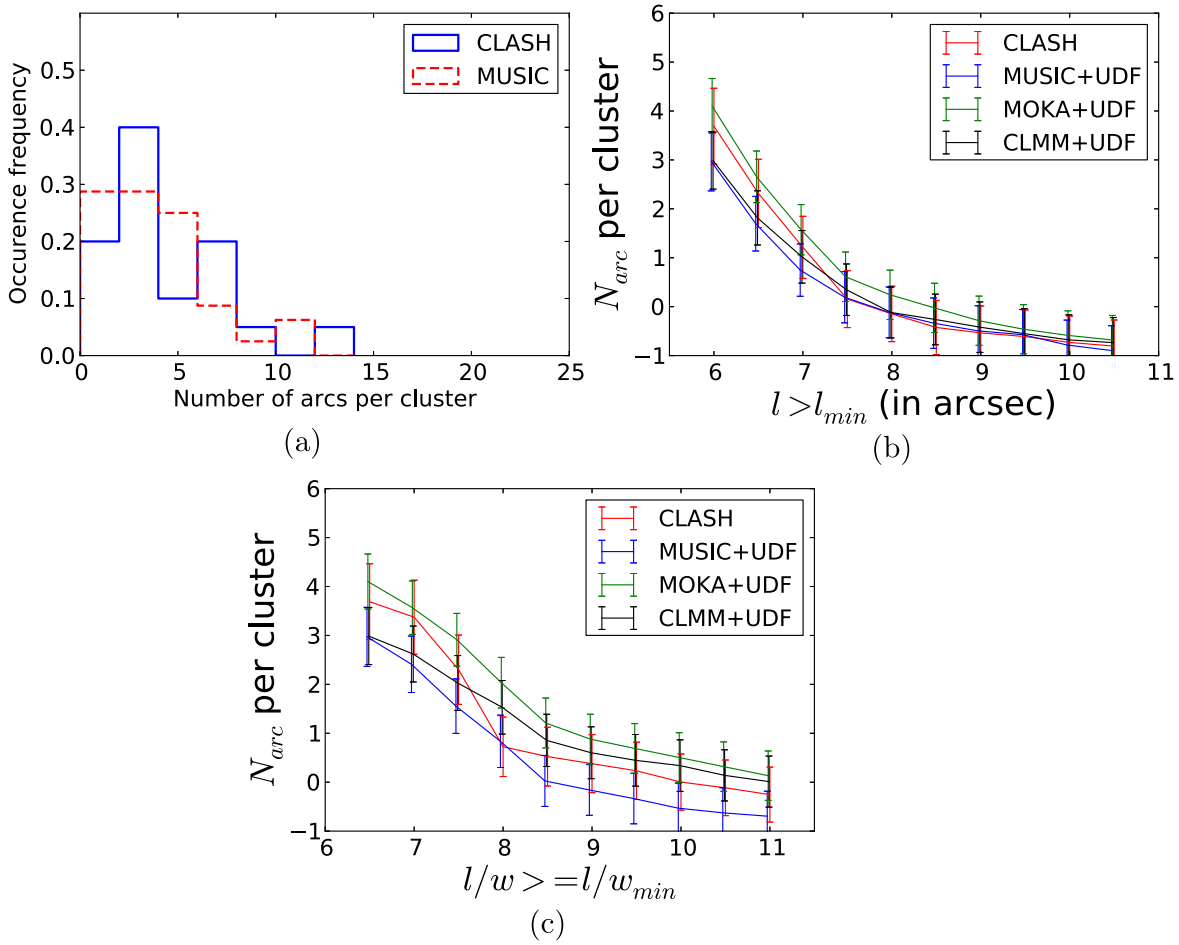

Figure 18. (a) Comparison of the number distribution between the CLASH sample and MUSIC sample. (b) Lensing efficiency as a function of $l_{\rm min}$ for arcs with $l/w \geqslant 7$ for different samples. (c) Lensing efficiency as a function of $l/w_{\rm min}$ for arcs with $l \geqslant 6''$ for different samples.

Table 4
Comparison of Lensing Efficiency between Observation and Simulation

Parameter	Lensing Efficiency	Difference relative to CLASH X-Ray-selected Sample
Observation (X-ray-selected sample)	4 ± 1	...
Observation (high-magnification sample)	5 ± 1	0.7σ
CLMM + UDF z-distn	3 ± 1	0.7σ
CLMM + ($z_s = 1$)	2 ± 1	1.4σ
CLMM + ($z_s = 2$)	3 ± 1	0.7σ
MOKA + UDF z-distn	4 ± 1	...
MOKA + ($z_s = 1$) + (B13) *c–M*	2 ± 1	2.2σ
MOKA + ($z_s = 2$) + (B13) *c–M*	5 ± 1	0.7σ
MOKA + UDF z-distn + (N07) *c–M*	1 ± 1	2.2σ
MUSIC + UDF z-distn	3 ± 1	0.7σ

(105) from the Sloan Giant Arcs Survey (SGAS) and from the Second Red Sequence Cluster Survey (RCS2) and study the redshift distribution of the arcs. They find that arcs with $g \leqslant 24$ have a median redshift of $z_s \sim 2$. Bayliss (2012) claims that the arc statistics problem can be solved by adopting their measured redshift distribution and using the scaling of the optical depth given in Wambsganss et al. (2004). However, Li et al. (2005) and Fedeli et al. (2006) show that the scaling of the optical depth is very different from what was assumed by Wambsganss et al. (2004) and that the Wambsganss et al. (2004) assumption that the magnification is a good measure for the l/w ratio of an arc is not justified in detail. Furthermore, it is unclear whether the arc identification used by Bayliss (2012) (e.g., by curvature radius of arcs and by visual inspection) might bias the selection in favor of luminous and highly curved arcs. If so, the corresponding arc abundance and redshift distribution could also possibly be biased.

Our results show that the simulations performed with either a UDF redshift distribution or a delta function redshift distribution at $z_s = 2$ give very similar arc abundances. When we change the redshift distribution of the background sources to a delta function at $z_s = 1$, the arc abundance drops by a factor of 2 rather than the order-of-magnitude change in the arc abundance noted in some previous studies (e.g., Wambsganss et al. 2004). The factor of 2 change is consistent with Horesh et al. (2005, 2011), who also used UDF images as background sources to perform the ray-tracing. Horesh et al. (2005) used

the same simulated clusters at $z_c = 0.2$ as used in B98 to lens the UDF sources and found an arc abundance that was 3 times higher than that in B98. They attributed this overabundance to the use of a source number density that was 3.2 times higher than that in B98. They found that changing the source redshift distribution from a delta function at $z_s = 1$ to a realistic UDF distribution results in only a small change in the final arc abundance. These results suggest that the redshift distribution does not have a major impact on the final arc abundance unless one selects a distribution that significantly underpopulates galaxies in the $z > 1$ range.

The MUSIC-simulated halos do not have BCGs at the center and do not implement complex gaseous physics. However, Killedar et al. (2012) have compared the arc production efficiency of the adiabatic simulations with some more sophisticated simulations that include effects such as gas cooling, star formation, and feedback from active galactic nuclei and supernova+galactic winds. The comparable results indicate that the implementation of baryonic physics will probably not lead to a significant change in the arc abundance derived from simulations without such processes.

Previous studies have already revealed the correlation between the lensing cross section and the Einstein radius, $\theta_{E,\mathrm{eff}}$, from N-body simulation (Meneghetti et al. 2011) and the semianalytic calculations (Redlich et al. 2012). Our study confirms this correlation as reflected by the dependence of the number of arcs per cluster on $\theta_{E,\mathrm{eff}}$, as shown in Figure 16(d). The relation between the MOKA cluster lensing efficiency and $\theta_{E,\mathrm{eff}}$ in our study is well fitted by a linear relation in log–log plane with a slope of 1.54 ± 0.08, which is flatter than the slope 1.79 ± 0.04 in Meneghetti et al. (2011) and 2.4 ± 0.04 in Redlich et al. (2012). The detection of this correlation in our MOKA simulations is due to the relatively large size of the MOKA cluster sample (640 simulated clusters), whereas the CLASH sample is too small to robustly unveil this correlation. For the arc abundance of ~5 per cluster, the fractional error for an ensemble of 32 realizations is $1/\sqrt{5 \times 32} \sim 8\%$. Therefore, to measure the correlation observationally to 10% and to detect a ~15% deviation from such correlation, we need $\frac{\times(1\,/\,0.1)^2}{5} = 20$ clusters in each mass bin, and we probably need a cluster sample with size ~ 200 if 10 different mass bins are expected.

We are able to identify the relative significance of several key physical effects that contribute to the arc abundance enhancement. As Table 4 shows, varying the source redshift distribution leads to, at most, a factor of 2 variation in the arc abundance. Variation of the c–M relations will affect the matter distribution of the inner cluster core and, hence, lead to variations in the arc abundance. Using several recent estimates of the c–M relation (Neto et al. 2007; Bhattacharya et al. 2013) results in variations of the arc abundance by up to a factor of ~4–5. Using the most recent estimates of the c–M relation in simulations appears to produce excellent agreement with the observed arc abundance. However, quantities such as mass and concentration alone are not sufficient to reflect the likely complex dependencies of the arc abundance on various effects. As shown in Figures 16(b) and (c), the arc abundance fails to exhibit a strong dependence on either the concentration or the cluster mass alone, for both the CLASH and MOKA samples. By contrast, the effective Einstein radius, $\theta_{E,\mathrm{eff}}$, is a good indicator of the lensing efficiency.

Given our results, even without fully understanding the cosmological dependence of the arc abundance, we could still conclude that the initial "arc statistics problem" appears to have been largely due to inadequate modeling of the mass distributions of the clusters and, secondarily, due to inadequate modeling of the background source number density and redshift distribution. In addition, the previous use of mostly visual identification of arcs may have resulted in an inadequate modeling of the false positive contamination rate and completeness corrections. We can divide the contributions from different physical effects on cluster lensing efficiency into three general categories: the cluster abundance, the background source redshift distribution, and the individual cluster lensing cross section. Our study would suggest that the lensing efficiency is more strongly dependent on the individual cluster lensing cross sections than on the source redshift distribution. However, different cosmology could alter both the cluster abundance and the individual cluster lensing cross sections, and the relative significance of such factors has not been explored in this study given the small cluster sample size. Future large cluster surveys (e.g., DES, LSST, Euclid, WFIRST) will definitely help to answer this question. We suspect that two other related problems in lensing, the overconcentration problem and Einstein radii problem, where it has been found that some real clusters at intermediate redshift have denser cores than clusters of similar mass produced in simulations (Broadhurst & Barkana 2008; Oguri & Blandford 2009; Richard et al. 2010; Sereno et al. 2010; Merten et al. 2015) and where some real clusters have larger Einstein radii than expected in standard ΛCDM cosmology, may well be due to a combination of insufficiently accurate cluster simulations and observational sample selection effects.

10. SUMMARY

We have carried out an observational and theoretical study of the arc statistics problem in clusters of galaxies. We have devised an automated arc finder to efficiently and objectively detect arcs. We test our arc finder using a large number of simulated cluster images and have quantified the incompleteness and false positive rate in arc detection. We also investigate how image noise affects the shape determination of the arcs and statistically correct for the observed elongation bias. We run our arc-finding algorithm on 20 X-ray-selected CLASH clusters and five high-magnification CLASH clusters. After correcting for arc shape elongation bias, incompleteness, and false positive rate, we find a large arc ($l/w > 6.5$ and $l \geqslant 6''$) lensing efficiency of 4 ± 1 arcs per cluster and 5 ± 1 arcs per cluster, respectively, for the X-ray-selected and high-magnification-selected CLASH samples.

We simulate mock clusters using both the MOKA semianalytic cluster generator and the MUSIC-2 N-body results. In both cases, we focus on simulated clusters that have the same mass and redshift range as the CLASH clusters. For the MOKA simulations, we use ray-tracing to create 640 simulated cluster realizations with the F775W UDF image as the same background source. For the simulations extracted from the high-resolution, hydrodynamical simulations (MUSIC), we identify halos that, in addition to having similar redshifts and virial masses as the CLASH clusters, are also selected to have similar X-ray morphologies to those of the CLASH clusters. We find a lensing efficiency of 4 ± 1 arcs per cluster in the MOKA simulations and 3 ± 1 arcs per cluster in

the MUSIC simulations. These lensing efficiencies both match the observed lensing efficiency of 4 ± 1 arcs per cluster. We also study the arc abundance dependence on the cluster redshift by splitting the sample into two bins divided at the median sample redshift of $z_{\rm median} = 0.352$ and find no significant differences in either the overall lensing efficiency or arc redshift distributions. The dependence of the MOKA and MUSIC lensing efficiencies on $l_{\rm min}$ and $l/w_{\rm min}$ also matches that seen in the observed CLASH ones.

For the future, the relatively short running time (less than 5 minutes for images with 3000×3000 pixels) of our arc finder allows us to perform large-scale "blind" searches for giant arcs in various other surveys, especially those with moderately high-angular resolution such as WFIRST and Euclid. Moreover, continued study of the correlation between the arc abundance and the $\theta_{E,\rm eff}$ should be conducted to assess just the reliability of using arc abundance (which is an observable) as a predictor of $\theta_{E,\rm eff}$.

We thank the referee for providing helpful comments and suggestions that significantly improved the paper. We thank Carlo Giocoli for making the MOKA code accessible and for his generous help in simulating the clusters. We thank the MUSIC group for also providing us with simulated cluster data sets. We acknowledge Matthias Bartelmann, Dan Coe, Colin Norman, and Brice Menard for many useful discussions. B.X. is supported by NASA funding received for the CLASH Multi-Cycle Treasury Program (*HST*-GO-12065). A.Z. is supported by NASA through Hubble Fellowship grant #*HST*-HF2–51334.001-A awarded by STScI. J.M. is supported by the People Programme (Marie Curie Actions) of the European Union Seventh Framework Programme (FP7/2007–2013) under REA grant agreement number 627288. The results in this paper are based on observations made with the NASA/ESA *Hubble Space Telescope*. The Space Telescope Science Institute is operated by the Association of Universities for Research in Astronomy, Inc., under NASA contract NAS 5-26555.

APPENDIX A
INTEGRATED QUANTIZED INTENSITY DIFFERENCE CRITERION

The following appendices provide further details about the arc finder algorithm. Specifically, we provide short summaries of the key steps performed to go from the initial science image to the final arc catalog. We begin by convolving our *HST* images with a square top-hat kernel with an edge dimension of $0\farcs065$ to modestly enhance the contrast of the faint and thin arcs. Most source detection algorithms work in intensity space, which means that the performance of these algorithms largely depends on how the detection threshold is chosen. A higher threshold will yield a catalog with lower completeness for faint objects, while a lower threshold will lead to less precise segmentation and a higher false positive rate. To avoid the nontrivial determination of an optimal detection threshold, we focus on three very general properties of giant arcs:

1. Giant arcs, like all real astronomical sources, have a net positive amount of flux on average after subtracting off a suitable background level.
2. Giant arcs have substantial angular lengths.
3. Giant arcs are highly elongated objects.

The above general properties imply that, on average, the intensity difference between the pixels belonging to the arc should be positive and the elongated and distorted morphologies of arcs should also be reflected in the angular distribution of these intensity differences. Use of the nonparametric intensity differences has a genuine advantage in the arc detection game: we can, in principle, detect faint structures almost as easily as bright structures. For this key reason, we perform the primary arc detection process in intensity difference space. To do this, we first lay down a grid of points on the smoothed image, at spatial scale n, that is somewhat larger than the arc widths we wish to find. At each grid point we then determine whether each of its eight adjacent grid points (up, down, left, right, upper left, upper right, lower left, lower right) is brighter or fainter than this pixel. We quantify this local set of flux differences by assigning a value of $+1$ for a positive difference (the central pixel at grid position (i, j) is brighter than a given surrounding pixel) and a value of -1 for a negative difference (the central pixel at grid position (i, j) is fainter than a given surrounding pixel). We sum up these values for all eight directions. A grid point that was brighter than all of its surrounding grid points would thus have a final value of $+8$. A grid point that was brighter than six of its surrounding grid points would have a final value of $6–2 = +4$. And so on. As arcs are highly elongated, pixels lying along the ridge line of an elongated arc will tend to have at least 4 or 5 adjacent pixels that are fainter than those at a given grid position. The value assigned to these pixels will thus be at least 2 or higher $(5–3 = 2)$. In general, the brighter pixels in an arc will tend to have higher integrated quantized intensity difference values than the fainter pixels. Given that some giant arcs may have complex intensity profiles, we set the threshold for the integrated quantized intensity difference to be the lowest positive value, which is $+2$. If we adopt a higher positive threshold, we find that some complex arcs are segmented into several smaller arc detections. The threshold of $+2$ is the most conservative in maintaining the overall structural shape of the arc candidates. We note that the exact choice of threshold value, however, does not significantly impact the contents of the final sample of large ($l \geqslant 6''$) and highly elongated ($l/w \geqslant 7$) arc candidates. The effect of the quantized intensity difference threshold is primarily on the number of small and less elongated sources in the initial detection process.

Choosing a proper grid spacing scale, n, is important. Generally, the spacing scale n should be larger than the typical arc's width, and it should be neither too large nor too small, to avoid extending the grid points to nearby bright structures or limiting the grid points around the arc rigid lines. To determine the scale, we visually select 58 giant arcs from our CLASH F814W images and manually measure the arcs' FWHM in the direction perpendicular to their ridge lines.[14] Figure 19 shows the distribution of the preselected arc's FWHM. Note that the median value of these 58 arcs is $0\farcs33$ and most of the arcs' widths are less than $0\farcs72$. In principle, we should traverse as many grid scales as possible to optimize the detection of the arcs, which is computationally expensive. We adopt two different scales, $0\farcs39$ and $0\farcs78$, to make sure that both narrow and wider arcs can be effectively detected in a relatively short computational time. The results based on each scale are combined as the input to the next step.

[14] To measure the FWHM, we first draw a line crossing the intensity maxima that is perpendicular to the arc's ridge line and then use a Gaussian profile to fit the intensity of pixels that fall on the line. We approximate the Gaussian FWHM as the FWHM of the arc.

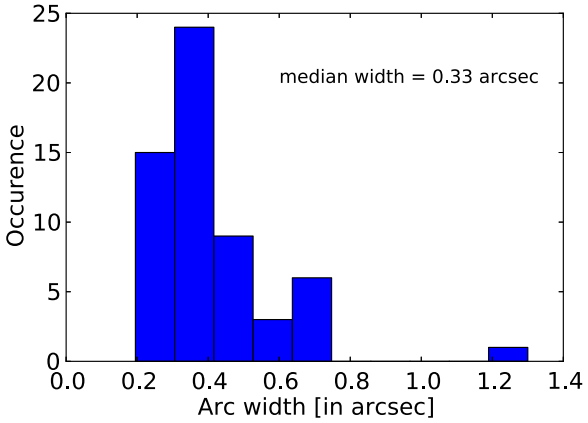

Figure 19. FWHM distribution of the preselected 58 giant arcs from CLASH F814W images. The median FWHM is around $0\farcs33$, and most of the arc widths are less than $0\farcs72$. The exception among this sample is from the cluster MACS 1206, which includes a giant arc with width $\sim 1\farcs3$.

As noise pixels may have regions with zero-valued or negative integrated quantized intensity difference,[15] another obvious advantage is that we are able to effectively clip out noise pixels and make the arc detection task significantly easier, even in the presence of a bright diffuse background, as might be encountered in the halo of a bright foreground cluster galaxy.

APPENDIX B
THE LOCAL INTENSITY DIFFERENCE CRITERION

In certain regions (especially in the inner cores of bright galaxies), applying the integrated quantized intensity difference criteria only will leave the segments with the diffraction pattern (see Figure 20(a)). To suppress these effects, we apply another criterion by comparing the intensity of the central pixel with the mean value of all 8 adjacent pixels over the image. The selected pixels should satisfy the two criteria below:

$$\sum_{l,m\in(-n,0,n)} \mathrm{SIGN}(I(i,j) - I(i+l, j+m)) \geqslant 2, \quad (4)$$

$$\sum_{l,m\in(-n,0,n)} (I(i,j) - I(i+l, j+m)) > 0. \quad (5)$$

Figures 20(b) and (c) show the integrated quantized intensity difference maps of MACS 0717 before and after applying the above criteria. We can see that the number of diffraction artifacts in the image is significantly reduced.

APPENDIX C
INITIAL IMAGE SEGMENTATION

To identify specific arcs, we need to locate regions of contiguous grid points in the integrated quantized intensity difference map with sums in excess of +2. We have now replaced the challenge of finding objects in intensity space with the task of finding contiguous regions in this quantized intensity difference space. We avoid using any global selection criterion on number density since the number density varies largely across the whole image. Hence, the contiguous regions are selected by their local number density of the grid points in the quantized intensity difference space. Based on the simple fact shown by Figure 20(d), if the contiguous region is enclosed by circle S1, the local averaged number density inside S1 must be larger than that inside circle S2, which has the same center as S1 but a larger radius. The details of contiguous regions' selection are as follows: (1) we make three convolved images using three spherical uniform kernels (k1, k2, and k3) with increasing size ($0\farcs52$, $1\farcs04$, and $1\farcs56$); (2) we subtract an image convolved with a broader kernel from one convolved with a narrower kernel, to obtain two residual images (k2–k1, k3–k2); (3) we then select all the pixels that have positive values in both residual images.

The selected contiguous regions include a few small and less elongated blobs that are not real sources. We set an area threshold $A > 100$ pixels and an eccentricity[16] threshold $e > 0.85$ to remove these artifacts. As shown in Figure 20 (b), the noise has been suppressed and most giant arcs have been retained.

APPENDIX D
SUPPRESSION OF DIFFRACTION SPIKES

Diffraction spikes from bright stars are the features likely to account for most of the false positive detections. The normal way to remove the star spikes is to locate the position of bright stars and then manually mask out the diffraction pattern. Here we adopt a different approach that eliminates the need to know the position of the bright stars or the direction of the spikes in advance.

Our approach is to merge the diffraction spikes with each associated star and eliminate the combined source as a whole. To do this, we enhance the strong intensity gradients near bright stars and their diffraction spikes by applying unsharp masking. The unsharp masking enhances the peak and dampens the wings of the intensity distribution. As a result, some dark halos can be observed around the stars or bright elliptical galaxies, which are shown in Figure 21(a). Empirically, we note that most of the pixels belonging to the dark halo regions in CLASH data tend to have an intensity value lower than $-0.01 e^{-}s^{-1}$, and we use this intensity as a threshold to identify these halos. We then dilate the segmentation boundaries around a dark halo in all directions to fill the gaps between the segments (Figure 21(b)) and combine the "dilated" images with the initial segmentation image obtained in Appendix C (Figure 21(c)). Most of the diffraction spikes merge with the segments of their mother stars as a result of performing this combination. We then label all the connected components[17] in the combined image and calculate the maximum pixel intensity of each labeled connected component. Stars typically have maximum intensity values greater than $10 e^{-}s^{-1}$, while other objects barely have the maximum intensity value larger than $2 e^{-}s^{-1}$; therefore, we can

[15] For noise pixels, if their distributions are independent, the integrated quantized intensity difference should be equal to 0.

[16] The eccentricity here is equal to the eccentricity of the ellipse that has the same second moments as the measured object.

[17] Whether a pixel connects to its neighbors or not is characterized by the pixel connectivity. Usually there are two types of connectivity: four-connected and eight-connected. Four-connected pixels are connected horizontally and vertically, or diagonally; eight-connected pixels are connected horizontally, vertically, and diagonally. In terms of pixel coordinates, in the four-connected case, every pixel that has the coordinates $(x \pm 1, y)$ or $(x, y \pm 1)$ is connected to the pixel at (x, y); in the eight-connected case, in addition to four-connected pixels, each pixel with coordinates $(x \pm 1, y \pm 1)$ or $(x \pm 1, y \pm 1)$ is connected to the pixel at (x, y). In this paper, all the adjacent eight-connected pixels are considered to belong to the same connected component.

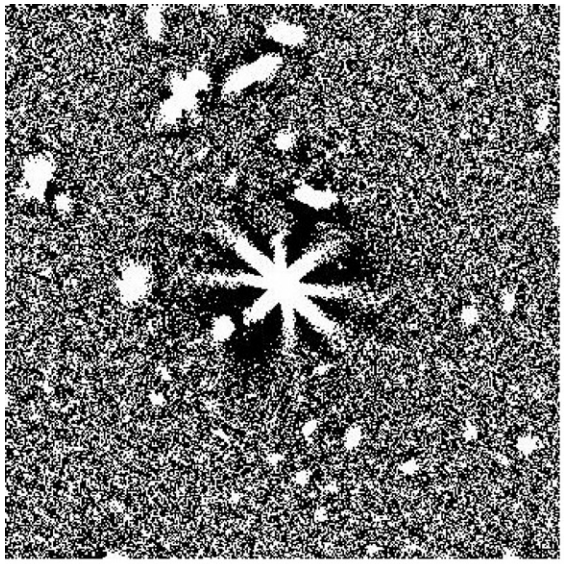

(a) Segment with the diffraction pattern

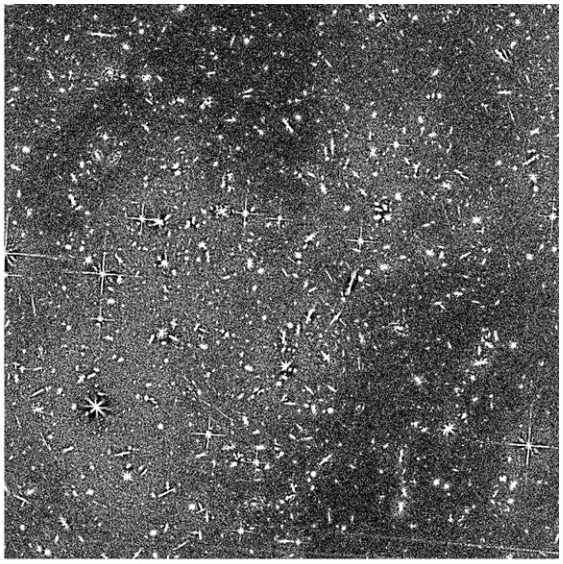

(b) Image before applying the local average criteria

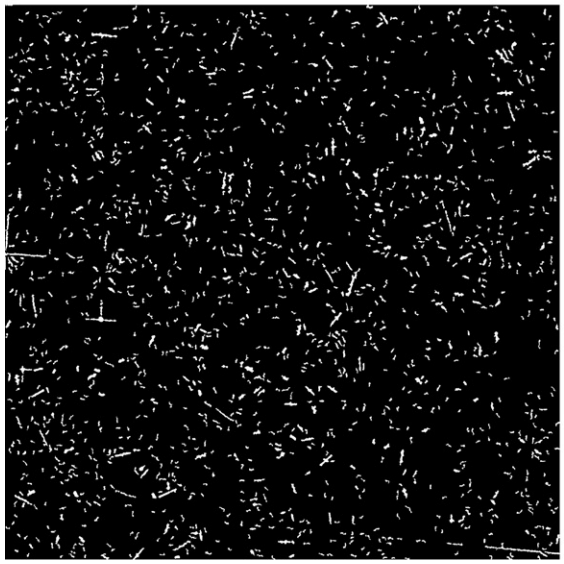

(c) Image after applying the local average criteria

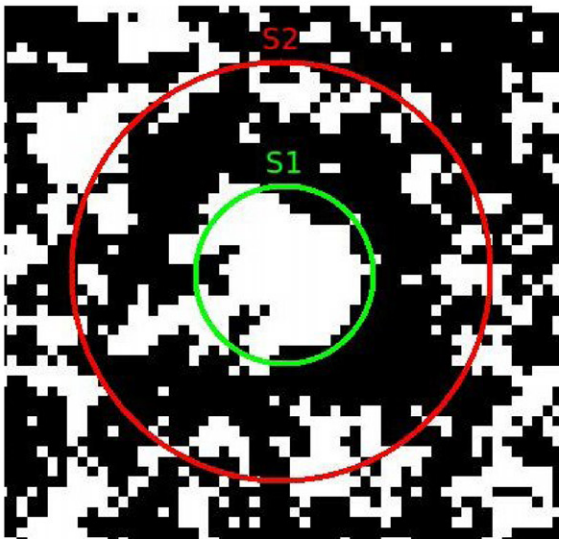

(d) Local contiguous regions selection

Figure 20. (a) Segment with the diffraction pattern that needs to be suppressed by the local average criteria; (b, c) integrated quantized intensity difference map of the MACS 0717 F814W image, before and after applying the local average criteria, respectively; (d) idea of local selection of contiguous regions: to draw circles with different size on each pixel and calculate the average number density within the circles, and select those grid points that have higher average number density within smaller circles.

conservatively set $10e^{-}s^{-1}$ as the threshold to remove those bright stars along with the diffraction spikes (Figure 21(d)).

APPENDIX E
FINAL IMAGE SEGMENTATION

The initial segmentation boundaries for objects detected in intensity difference space tend to have systematically larger surface area than the corresponding segmentation boundaries in pixel intensity space. Hence, we refine the initial segmentation map to correct this small effect. We first define, for each detected segment, a "bounding box" that spans the region from the minimum x, y coordinates to the maximum x, y coordinates. We then iteratively clip out pixels with very high (low) intensity within this box until the pixel intensity reaches convergence at $\pm 3\sigma$ around its median value. We then estimate the local background and noise level within the box. Since faint arcs are most likely missed or broken into small arclets at a high detection threshold, we set the threshold for the re-

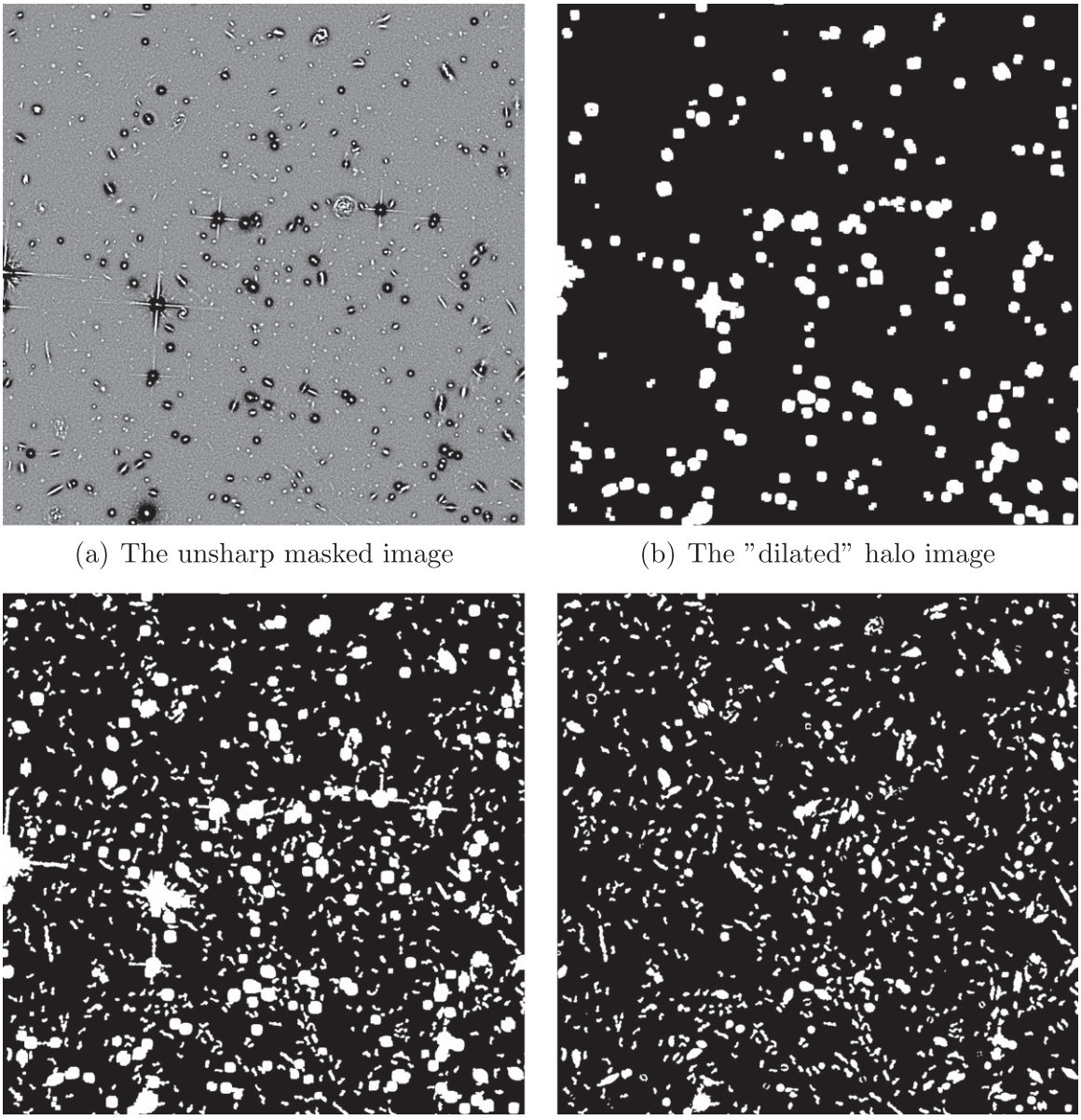

(a) The unsharp masked image (b) The "dilated" halo image

(c) The halo image combined with the detection image (d) The image with the star spikes removed

Figure 21. Black halo regions are identified from the unsharp masked image by setting the threshold to $-0.01e^{-}s^{-1}$. The halo segments are "dilated" (expanded) and combined with the normal detection image so that the stars start to merge with the diffraction spikes. Most of the diffraction spikes can be removed by setting the maximum intensity value of the labeled segments less than $10e^{-}s^{-1}$.

segmentation to be proportional to the object's estimated local S/N. Hence, objects with low surface brightness will be remapped using a lower detection threshold than that used for brighter objects, allowing all sources to achieve their best segmentation (see Figure 22).

APPENDIX F
UTILIZATION OF THE LENGTH, LENGTH-TO-WIDTH RATIO, AND PERIMETER-TO-LENGTH RATIO

Once all images are processed through the preceding steps, we can begin the arc identification process. We identify giant arcs from among all detected sources primarily by their large ellipticity. For each source, we calculate the total area, perimeter length, and position of the peak intensity from the distribution of all the connected pixels.[18] Using the coordinates of the pixel with the peak intensity value in a given source, we locate the farthest point away from that maximum that is still within the boundaries of the source. We also locate the farthest point away from that point, then calculate the sum of the distances from these two points to the peak pixel position, and take this distance as the length of the segment. There are many ways to define the width of the segment: the image segments can be fitted by simple geometrical figures such as ellipse,

[18] We utilize `ndimage` (a Python image processing module) to quickly calculate the mentioned parameters of the detected objects.

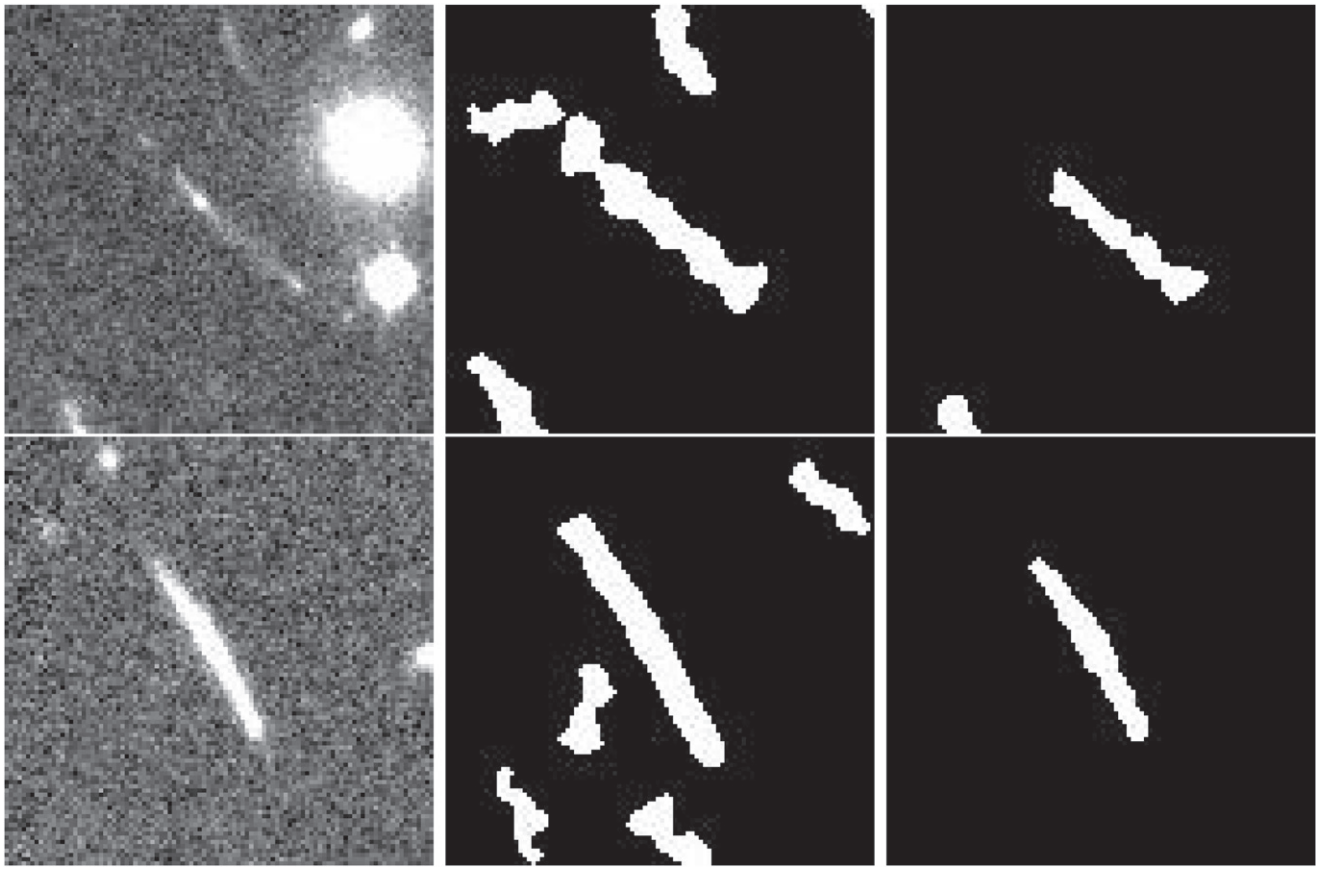

Figure 22. Left: original images of arc; middle: primary segmentation; right: images after the segmentation re-determination. The local background and noise level within the box are estimated, and the detection threshold is set to be proportional to its S/N level.

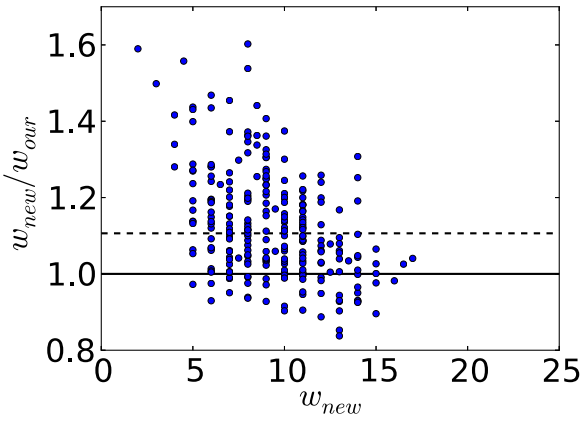

Figure 23. Comparison of two definitions of the width of arc: the y-axis is the ratio of the newly defined width to our width; the x-axis is the newly defined width. The solid line represents $w_{\rm new} = w_{\rm our}$, while the dashed line denotes the median value of the ratio of the two widths.

circles, rectangles, and rings (Miralda-Escude 1993; Bartelmann & Weiss 1994), and therefore the width of the segment is approximated by the minor axis of the ellipse, the radius of the circle, the smaller side of the rectangle, or the width of the ring. Dalal et al. (2004), Horesh et al. (2005), and Hennawi et al. (2007) approximated the width by dividing the area by its length; Meneghetti et al. (2008) proposed a more robust way to measure the width, by traversing the width profile of the arc and approximating the arc width as the median value of the profile. In this study, considering the computational efficiency, we adopt the former method: i.e., all the giant arcs are treated as rectangles and width = area/length, to determine the width of the segment in this paper. To test whether this definition of width will introduces bias in the measurement of l/w, we use the approach in Meneghetti et al. (2008) to re-calculate the width of all the detected arcs and compare with those in the former definition. Figure 23 shows the comparison of the ratio of two widths with the newly defined width. The dashed line denotes the median value of the ratio, which is about 10% higher than that in our definiton. Therefore, our l/w (width) measure may be slightly biasing high (low).

The final step is to remove those detected segments that are not very likely to be large lensed galaxies by requiring objects to satisfy three additional criteria:[19] (1) their perimeter-to-length ratio must be $\geqslant$3; (2) their minimal length must be greater than a fixed value, which is discussed in Section 3.2; (3) their minimal length-to-width ratio must be greater than a fixed value, which is determined in Section 3.2. Criterion 1 eliminates elongated objects with irregular morphology, and criterion 2 both maintains the consistency with the concept of the "giant" arcs and prevents the domination of the spurious detection, as we discuss in Section 3.1. We include all objects that satisfy these three constraints in our final arc candidate catalog.

[19] In this study, we do not need to specify the orientation of the giant tangential arcs relative to the cluster center. This allows us to apply our algorithm to less relaxed clusters that may not have a well-defined center.

REFERENCES

Alard, C. 2006, arxiv:astro-ph/0606757
Bartelmann, M., Huss, A., Colberg, J. M., Jenkins, A., & Pearce, F. R. 1998, A&A, 330, 1
Bartelmann, M., Meneghetti, M., Perrotta, F., et al. 2003, A&A, 409, 449
Bartelmann, M., & Weiss, A. 1994, A&A, 287, 1
Bayliss, M. B. 2012, ApJ, 744, 156
Bayliss, M. B., Gladders, M. D., Oguri, M., et al. 2011, ApJL, 727, L26
Benítez, N. 2000, ApJ, 536, 571
Benítez, N., Ford, H., Bouwens, R., et al. 2004, ApJS, 150, 1
Bhattacharya, S., Habib, S., Heitmann, K., & Vikhlinin, A. 2013, ApJ, 766, 32
Biffi, V., Sembolini, F., De Petris, M., et al. 2014, MNRAS, 439, 588
Boldrin, M., Giocoli, C., Meneghetti, M., et al. 2015, arXiv:1505.03515
Broadhurst, T. J., & Barkana, R. 2008, MNRAS, 390, 1647
Coe, D., Benítez, N., Sánchez, S. F., et al. 2006, AJ, 132, 926
Dalal, N., Holder, G., & Hennawi, J. F. 2004, ApJ, 609, 50
D'Aloisio, A., & Natarajan, P. 2011a, MNRAS, 411, 1628
D'Aloisio, A., & Natarajan, P. 2011b, MNRAS, 415, 1913
Fedeli, C., Bartelmann, M., Meneghetti, M., & Moscardini, L. 2008, A&A, 486, 35
Fedeli, C., Meneghetti, M., Bartelmann, M., Dolag, K., & Moscardini, L. 2006, A&A, 447, 419
Fioc, M., & Rocca-Volmerange, B. 1997, A&A, 326, 950
Flores, R. A., Maller, A. H., & Primack, J. R. 2000, ApJ, 535, 555
Furlanetto, C., Santiago, B. X., Makler, M., et al. 2013, A&A, 549, 80
Gao, L., White, S. D. M., Jenkins, A., Stoehr, F., & Springel, V. 2004, MNRAS, 355, 819
Gardini, A., Rasia, E., Mazzotta, P., et al. 2004, MNRAS, 351, 505
Giocoli, C., Meneghetti, M., Bartelmann, M., et al. 2012, MNRAS, 421, 3343
Gottlöber, S., & Yepes, G. 2007, ApJ, 664, 117
Grogin, N., Kocevski, D., Faber, S. M., et al. 2011, ApJS, 197, 35
Hennawi, J. F., Dalal, N., Bode, P., & Ostriker, J. P. 2007, ApJ, 654, 714
Hilbert, S., Metcalf, R. B., & White, S. D. M. 2007, MNRAS, 382, 1494
Hilbert, S., White, S. D. M., Hartlap, J., & Schneider, P. 2008, MNRAS, 386, 1845
Horesh, A., Maoz, D., Ebeling, H., Seidel, G., & Bartelmann, M. 2010, MNRAS, 406, 1318
Horesh, A., Maoz, D., Hilbert, S., & Bartelmann, M. 2011, MNRAS, 418, 54
Horesh, A., Ofek, E. O., Maoz, D., et al. 2005, ApJ, 633, 768
Jing, Y., & Suto, Y. 2002, ApJ, 574, 538
Jullo, E., Natarajan, P., Kneib, J.-P., et al. 2010, Sci, 329, 924
Killedar, M., Borgani, S., Meneghetti, M., et al. 2012, MNRAS, 427, 533
Klypin, A., Kravtsov, A. V., Bullock, J. S., & Primack, J. R. 2001, ApJ, 554, 903
Koekemoer, A., Faber, S. M., Ferguson, H., et al. 2011, ApJS, 197, 36
Kravtsov, A. V., Klypin, A. A., & Khokhlov, A. M. 1997, ApJS, 111, 73
Lenzen, F., Schindler, S., & Scherzer, O. 2004, A&A, 416, 391
Li, G.-L., Mao, S., Jing, Y. P., et al. 2005, ApJ, 635, 795
Li, G.-L., Mao, S., Jing, Y. P., et al. 2006, MNRAS, 372, 73
Meneghetti, M., Bartelmann, M., Dolag, K., et al. 2005, A&A, 442, 413
Meneghetti, M., Bartelmann, M., & Moscardini, L. 2003, MNRAS, 346, 67
Meneghetti, M., Bolzonella, M., Bartelmann, M., Moscardini, L., & Tormen, G. 2000, MNRAS, 314, 338
Meneghetti, M., Fedeli, C., Pace, F., Gottlóber, S., & Yepes, G. 2010, A&A, 519, 90
Meneghetti, M., Fedeli, C., Zitrin, A., et al. 2011, A&A, 530, 17
Meneghetti, M., Melchior, P., Grazian, A., et al. 2008, A&A, 482, 403
Meneghetti, M., Rasia, E., Vega, J., et al. 2014, ApJ, 797, 34
Merten, J., Meneghetti, M., Postman, M., et al. 2015, ApJ, 806, 4
Miralda-Escude, J. 1993, ApJ, 403, 497
Neto, A. F., Gao, L., Bett, P., et al. 2007, MNRAS, 381, 1450
Oguri, M., & Blandford, R. 2009, MNRAS, 392, 930
Oguri, M., Lee, J., & Suto, Y. 2003, ApJ, 559, 572
Planck Collaboration, Ade, P. A., Aghanim, N., Armitage-Caplan, C., et al. 2014, A&A, 571, A16
Postman, M., Coe, D., Benitez, N., et al. 2012, ApJS, 199, 25
Puchwein, E., Bartelmann, M., Dolag, K., & Meneghetti, M. 2005, A&A, 442, 405
Puchwein, E., & Hilbert, S. 2009, MNRAS, 398, 1298
Redlich, M., Bartelmann, M., Waizmann, J.-C., & Fedeli, C. 2012, A&A, 547, 66
Richard, J., Smith, G. P., Kneib, J., et al. 2010, MNRAS, 404, 325
Rozo, E., Nagai, D., Keeton, C., & Kravtsov, A. 2008, ApJ, 687, 22
Seidel, G., & Bartelmann, M. 2007, A&A, 472, 341
Sembolini, F., Yepes, G., De Petris, M., et al. 2013, MNRAS, 429, 323
Sereno, M., Jetzer, P., & Lubini, M. 2010, MNRAS, 403, 2077
Springel, V. 2005, MNRAS, 364, 1105
Torri, E., Meneghetti, M., Bartelmann, M., et al. 2004, MNRAS, 349, 476
Umetsu, K., Medezinski, E., Nonino, M., et al. 2014, ApJ, 795, 163
Wambsganss, J., Bode, P., & Ostriker, J. P. 2004, ApJL, 606, L93
Wambsganss, J., Bode, P., & Ostriker, J. P. 2005, ApJL, 635, L1
Wuyts, S., Labbé, I., Schreiber, N. M. F., et al. 2008, ApJ, 682, 985
Zitrin, A., Fabris, A., Merten, J., et al. 2015, ApJ, 801, 44
Zitrin, A., Meneghetti, M., Umetsu, K., et al. 2013, ApJ, 762, 30